Environmental Science and Pollution Research (2020) 27:28649–28669
https://doi.org/10.1007/s11356-020-08729-w

ADVANCES IN ENVIRONMENTAL BIOTECHNOLOGY AND ENGINEERING 2018

Biological synthesis of iron nanoparticles using hydrolysates from a waste-based biorefinery

Leticia Romero-Cedillo[1,2] · Héctor M. Poggi-Varaldo[1,2] · Jaime Santoyo-Salazar[1] · Carlos Escamilla-Alvarado[3] · Yasuhiro Matsumoto-Kuwabara[1] · M. Teresa Ponce-Noyola[4] · Luz Bretón-Deval[5] · Miguel García-Rocha[1]

Received: 28 August 2019 / Accepted: 2 April 2020 / Published online: 28 April 2020

Abstract

The purpose of this work was to produce iron nanoparticles (Fe-NP) by microbial pathway from anaerobic bacteria grown in anaerobic fluidized bed reactors (AnFBRs) that constitute a new stage of a waste-based biorefinery. Bioparticles from biological fluidized bed reactors from a biorefinery of organic fraction of municipal solid wastes (that produces hydrolysates rich in reducing sugars) were nanodecorated (embedded nanobioparticle or nanodecorated bioparticle, ENBP) by biological reduction of iron salts. Factors "origin of bioparticles" (either from hydrogenogenic or methanogenic fluidized bed reactor) and "type of iron precursor salt" (iron chloride or iron citrate) were explored. SEM and high-resolution transmission electron microscopy (HRTEM) showed amorphous distribution of nanoparticles (NP) on the bioparticles surface, although small structures that are nanoparticle-like could be seen in the SEM micrographs. Some agglomeration of NPs was confirmed by DLS. Average NP size was lower in general for NP in ENBP-M than ENBP-H according to HRTEM. The factors did not have a significant influence on the specific surface area of NPs, which was high and in the range 490 to 650 $m^2\ g^{-1}$. Analysis by EDS displayed consistent iron concentration 60–65% iron in nanoparticles present in ENBP-M (bioparticles previously grown in methanogenic bioreactor), whereas the iron concentration in NPs present in ENBP-H (bioparticles previously grown in hydrogenogenic bioreactor) was more variable in a range from 8.5 to 62%, depending on the iron salt. X-ray diffraction patterns showed the typical peaks for magnetite at 35° (3 1 1), 43° (4 0 0), and 62° (4 0 0); moreover, siderite diffraction pattern was found at 26° (0 1 2), 38° (1 1 0), and 42° (1 1 3). Results of infrared analysis of ENBP in our work were congruent with presence of magnetite and occasionally siderite determined by XRD analysis as well as presence of both Fe^{+2} and F^{+3} (and selected satellite signal peaks) observed by XPS. Our results on the ENBPs hold promise for water treatment, since iron NPs are commonly used in wastewater technologies that treat a wide variety of pollutants. Finally, the biological production of ENBP coupled to a biorefinery could become an environmentally friendly platform for nanomaterial biosynthesis as well as an additional source of revenues for a waste-based biorefinery.

Keywords Anaerobic fluidized bed reactors · Biogenic synthesis · Biorefinery · Characterization · Embedded nanobioparticles · Hydrolysates

Responsible Editor: Santiago V. Luis

Electronic supplementary material The online version of this article (https://doi.org/10.1007/s11356-020-08729-w) contains supplementary material, which is available to authorized users.

✉ Héctor M. Poggi-Varaldo
r4cepe@yahoo.com; leticia.romero@cinvestav.mx

[1] Programa de Doctorado en Nanociencias y Nanotecnología, CINVESTAV del IPN, P.O. Box 17-740, 07000 Mexico City, Mexico

[2] Environmental Biotechnology and Renewable Energies Group, CINVESTAV del IPN, P.O. Box 14-740, 07000 Mexico City, Mexico

[3] Centre for Research on Biotechnology and Nanotechnology (CIByN), Faculty of Chemical Sciences, Engineering and Sustainable Bioprocesses Group, UANL, Parque de Investigación e Innovación Tecnológica, km 10 Autopista al Aeropuerto Internacional Mariano Escobedo, 66629, Apodaca, Nuevo León, Mexico

[4] Departamento de Biotecnología y Bioingeniería, CINVESTAV del IPN, Mexico City, Mexico

[5] Cátedras Conacyt - Instituto de Biotecnología, UNAM, Av. Universidad 2001, Chamilpa, 62210 Cuernavaca, Morelos, Mexico

Abbreviation

AnFBR	Anaerobic fluidized bed reactor
AnFBR-H	Anaerobic fluidized bed reactor producing biological hydrogen
AnFBR-M	Anaerobic fluidized bed reactor producing methane
BE	Binding energy
BET	Brunauer-Emmett-Teller, surface adsorption method
BP	Bioparticle
COD	Chemical oxygen demand
COD_i	Chemical oxygen demand at the start of biosynthesis process
COD_f	Chemical oxygen demand at the end of biosynthesis process
2,4-D	2,4-Dichlorophenoxy-acetic acid
db	Dry basis
DCA	Dichloroethane
DLS	Dynamic light scattering
EDS	Energy-dispersive spectroscopy
ENBP	Embedded nanobioparticle or nanodecorated bioparticle
ENBP-H	Embedded nanobioparticle from hydrogenogenic AnFBR-H
ENBP-M	Embedded nanobioparticle from methanogenic AnFBR-M
FWHM	Full width at half maximum of a peak in a given spectrum
GAC	Granular activated carbon
H	Source of ENBPs, i.e., from an AnFBR worked on dark fermentation regime
HRTEM	High-resolution transmission electron microscopy
HSP	Heat shock pretreatment
IR	Infrared spectroscopy
M	Source of ENBPs, i.e., from an AnFBR worked on methanogenic regime
MRI	Seeding or inoculating methanogenic reactor
NP	Nanoparticle
nZVI	Nanozero valent iron
OFMSW	Organic fraction of municipal solid wastes
PAC	Powdered activated carbon
PCE	Perchloroethylene
RI	Relative intensity
SAED	Selected area electron diffraction
SEM	Scanning electron microscopy
TCA	Trichloroethane
TCE	Trichloroethylene
VFA	Volatile fatty acids
VSS	Volatile suspended solids
wb	Wet basis
XPS	X-ray photoelectron spectroscopy
XRD	X-ray diffraction

Greek characters

ρ	Ratio of total volatile fatty acids (COD basis)-to-solvents (COD basis)
2θ	Angle between transmitted X-ray beam and reflected beam
η_{COD}	Efficiency of organic matter removal in terms of chemical oxygen demand

Introduction

Nanomaterials like metal oxide nanoparticles have been shown to be an efficient alternative for the remediation of several recalcitrant organochlorinated pollutants such as perchloroethylene (PCE) in municipal wastewater and groundwaters (Albergaria et al. 2010; USEPA 2006, 2017; Hennebel et al. 2009; Khin et al. 2012; Bretón-Deval and Poggi-Varaldo 2017; Bretón-Deval et al. 2013).

Indeed, in order to achieve higher efficiencies in the remediation of chlorinated compounds, several nanomaterials based on iron, silver, nickel, cobalt, and titanium, inter alia, have been used (Lohner and Spormann 2017; Machado et al. 2014). These nanomaterials have been shown to improve/stabilize the process of dehalogenation and often have allowed the recovery of nanoparticles for their reuse (Seabra et al. 2013).

On the other hand, when oxygen is not available in water, several bacterial strains grown in anaerobic and anoxic conditions can degrade chlorinated chemical compounds, usually by reductive dehalogenation (Staniland et al. 2009; Garibay-Orijel et al. 2005). Regarding degradation of chlorinated aliphatics, most of such bacteria are related to *Dehalobacter* and *Dehalococcoides* genuses (Bretón-Deval et al. 2016; Judger et al. 2016; Marzorati et al. 2007; Mayer-Blackwell et al. 2017). Several anaerobic bacteria use the organic chlorine(s) present in the organochlorinated compounds as final electron acceptor in a process known as reductive dehalogenation (Jacob and Suthindhiran 2016; Staniland et al. 2009; Sundaram et al. 2012; Yan et al. 2017).

Magnetite Fe_3O_4 is an iron oxide commonly used in environmental remediation of chlorinated compounds and is typically obtained by a coprecipitation technique based on a mixture of ferric and ferrous salts in the presence of $NaBH_4$ as a typical reductant (Laurent et al. 2008). Most of the research reported about iron nanoparticles (NP) by chemical synthesis is relatively well established (Chen et al. 2014; Corr et al. 2008). More recently, the efforts have been focused on implementing alternative methods in order to minimize or avoid the use of chemical agents and the discharges of toxic effluents (WHO 2000), as well as standardize the optimal concentration of nanoparticles in environmental processes (Thunugunta et al. 2015; Jiménez-Pérez et al. 2012).

Thus, biogenic methods are becoming increasingly used for the synthesis of iron NP (Bharde et al. 2006; Kaufmann and Lovley 2001). In the biosynthesis of magnetite is commonly found species of iron reducing bacteria such as *Geobacter metallireducens* (Lovley et al. 1993), *Shewanella oneidensis* (Fredrickson et al. 1998; Ross et al. 2007), *Thermoanaerobacter ethanolicus* (Roh et al. 2002), and *Magnetospirillum magnetotacticum* (Noguchi et al. 1999).

Iron reducing bacteria can use Fe(III) in oxidized state under anaerobic conditions as well as poorly secreted crystal Fe(II) in culture medium. Fe(II) in excess can be adsorbed as granular iron hydroxide and transformed into magnetite (Yeary et al. 2005). Magnetite synthesis can be favored by alkaline conditions (Eq. 1)

$$\left.\begin{array}{l} CH_3COO^- + 8Fe\ (OH)_3 \rightarrow 8Fe^{+2} + 2HCO_3^- + 15OH^- + 5H_2O \\ 2OH^- + Fe^{+2} + 2Fe\ (OH)_3 \rightarrow Fe_3O_4 + 4H_2O \end{array}\right\} \quad (1)$$

Typically, bacterial cytochromes are known to be involved in the nanosynthesis of magnetic NP. Gaspard et al. (1998) elucidated the reduction of Fe(III) by *Geobacter sulfurreducens*. This strain can generate electrons from oxidized NADH which are placed into 89 kDa cytochrome. Afterwards, they are transferred to the periplasmic space of 9 kDa cytochrome from which the electrons are used to reduce Fe(III) to Fe(II) through the 41 kDa cytochrome (Magnuson et al. 2001).

In recent years, Byrne et al. (2015) scaled up the biogenic process for magnetic nanoparticles by *Geobacter sulfurreducens*; they could produce up to 120 g of magnetite in 24 h. However, this process was carried out under optimal conditions using pure bacterial culture and electron donor and acceptor acetate and fumarate, respectively.

The emerging interest in developing sustainable and ecofriendly platforms are turning to the exploration of wastes that could substitute expensive raw materials and polluting nanosynthesis processes. About this approach, a wide variety of residues such as food, grapefruit, and rice husk wastes have been used (Piccinno et al. 2018; Satari and Karimi 2018; Vilaplana et al. 2010). Also, glass and plastic bag wastes were pretreated and recycled to produce engineered nanomaterials (Samaddar et al. 2018).

In the case of application of magnetite-based NPs in biorefinery processes, there are important potential benefits such as in situ recovery of the NPs which allows a continuous fermentation and separation of products and to reduce the washing time of production cycles, among others (Safarik et al. 2016). Also, hybrid iron nanoparticles such as NiFe exhibit another interesting application that consists of the sustainable hydrogenation of molecules from compounds such as glucose and xylose, which can be transformed to attractive products sorbitol and xylitol (Chieffi et al. 2014).

The objective of this work was to synthesize and characterize iron embedded nanobioparticles (ENBP) by biological means, using saccharified waste liquors (hydrolysates of the organic fraction of municipal solid waste, OFMSW) as well as anaerobic consortia anchored to bioparticles of fluidized bed bioreactors, in a waste-based biorefinery. We hypothesized that the hydrolysate would provide reducing power to the microbes in the bioparticles to effect iron reduction to magnetite. The experiment in our research evaluated the effects of "origin of bioparticles" (either BP from a methanogenic and hydrogenogenic fluidized bed reactors) and "type of precursor iron salt" (iron chloride and iron citrate) on the characteristics of Fe-NP.

Incidentally, but important, the synthesized ENBP could be used for treating groundwaters and wastewaters polluted with organochlorinated compounds and could become, hopefully, an additional source of revenues of waste-based biorefineries (Poggi-Varaldo et al. 2014; Escamilla-Alvarado et al. 2017).

Materials and methods

Experimental design

The experiment was arranged as a 2^2 factorial. The first factor was the "origin or source of the BP" (either from a hydrogenogenic fluidized bed bioreactor, AnFBR-H, or a methanogenic one, AnFBR-M). The second factor was the "type of precursor salts," either (i) ferric chloride 0.25 M or (ii) ferric citrate 0.1 M. The effects of the above cited factors on ENBP characteristics were explored. A summary of the experimental conditions in the four treatments of the experiments is shown in Table 1.

BPs from anaerobic fluidized bed reactors were sampled and transferred to serum bottles loaded either with (i) ferric chloride 0.25 M or (ii) ferric citrate 0.1 M, additionally supplemented with hydrolysate enough for initial 10 g L^{-1} or 16 g L^{-1} reducing sugars, and incubated at 37 °C for 7 days, leading to generation of nanodecorated bioparticles (herein

Table 1 Experimental conditions for nanodecoration of bioparticles previously grown in anaerobic bioreactors using iron salts and hydrolysates of the organic fraction of municipal solid wastes

Parameter	ENBP-H[a]	ENBP-M[b]
Reducing sugars initial concentration (g L^{-1})	16	10
Bioparticles (g_{wb})	10	10
Reaction volume (mL)	60	60
Precursor 1: ferric chloride (M)	0.25	0.25
Precursor 2: ferric citrate (M)	0.10	0.10

[a] Nanoparticles from embedded nanobioparticles from the hydrogenogenic bioreactor

[b] Nanoparticles from embedded nanobioparticles from the methanogenic bioreactor

after called embedded nanobioparticles, ENBP). All treatments received hydrolysates of OFMSW enough to give initial 10 and 16 g L^{-1} reducing sugars for the M and H ENBP, respectively.

Response variables of the characterization experiment were the size distribution, specific surface area, shape, iron content and speciation in NP of the ENBP, and the presence of magnetite and siderite. The experiment was run in two replicates. The control was granular activated carbon (GAC) uncolonized by anaerobic bacteria. The BPs withdrawn from AnFBR-H and AnFBR-M (10 g_{wb}) were added to the mixture of corresponding salt precursor and reducing sugars from hydrolysates in serum bottles (Table 1) for the biosynthesis of ENBP and incubated for 37 °C for 7 days.

Afterwards, the ENBPs were recovered from the liquor by centrifugation at 6000 rpm for 10 min and washed 5 times with ethanol. The solids were dried under N_2 inert atmosphere and then pulverized in a mortar for microscopic analysis.

Two lab-scale AnFBRs were supplemented with hydrolysates from OFMSW and operated in mesophilic regime. Both AnFBRs were loaded with GAC as a support material. Anaerobic consortia were grown on the GAC particles, leading to the formation of colonized bioparticles in the reactors. One AnFBR was targeted to bioH_2 generation (AnFBR-H), whereas the other one (AnFBR-M) was maintained in methanogenic regime.

Start-up and operation of the anaerobic reactors used in biological hydrogen and methane production fed with hydrolysate from the organic fraction of municipal solid waste

Two lab scales (AnFBR) were used for bioH_2 (AnFBR-H) and CH_4 production (AnFBR-M). The reactors were made with glass columns with an internal diameter of 4.5 cm and 185 cm height; their working volume was 2.8 L. Each reactor was loaded with 1 kg of granular activated carbon (GAC) with average diameter of 1 mm.

Both reactors were loaded with (at the start-up) and subsequently fed synthetic wastewater during operation. The composition of this wastewater was as follows (in mg L^{-1}): urea (125), $FeSO_4{\cdot}7H_2O$ (5), $CaCl_2$ anhydrous (47), $FeCl_3{\cdot}6H_2O$ (0.5), SeO_2 (0.07), $CoCl_2$ (0.08), KH_2PO_4 (85), Na_2HPO_4 (21.7), K_2HPO_4 (33.4), and $NaHCO_3$ (1000).

The pH for feedwater of the AnFBR-H was adjusted to 6.5 with HCl and supplemented with hydrolysates to give 16 g L^{-1} in reducing sugars; the pH of feedwater of the AnFBR-M was adjusted to 8.0 using NaOH and supplemented with hydrolysates to attain 10 g L^{-1} reducing sugars.

The inoculum for the AnFBR-H consisted of 500 g of the contents from a methanogenic reactor (MRI); this inoculum was subjected to heat shock pretreatment (HSP) (Escamilla-Alvarado et al. 2012, 2013) with the purpose of eliminating methanogenic archaea as well as favoring sporulation (and survival) of selected fermentative hydrogen bacteria (like those of the genus *Clostridium*). Afterwards, the AnFBR-H was treated similarly to the AnFBR-M described below.

The inoculum for AnFBR-M (500 g) was sampled from a methanogenic reactor (MRI) according to previous works (Moreno-Medina et al. 2017; Poggi-Varaldo et al. 2012). After the AnFBR-M received the first load of feedwater and inoculum, it was flushed with N_2 for 10 min in order to expel the atmospheric O_2 and generate anoxic conditions in the reactor. The recirculation pump was set at a flowrate of 240 mL min^{-1}.

Both reactors were kept in recirculation mode for 1 week without addition of feedwaters to foster the colonization of GAC particles.

Substrate preparation and detoxification

Hydrolysate from OFMSW was obtained by the method of acid hydrolysis (sulfuric acid 3%, 10:1 ratio) reported in a previous work (Hernández-Correa et al. 2017). In order to reduce the concentration of toxicants (phenolic compounds and furfural), the hydrolysate was subject to adsorption with powdered activated carbon (PAC) at 2% (w/v) for 2 h at 150 rpm. After this time, the hydrolysate was settled and further filtered using a Whatman paper filter no. 1 to separate the PAC.

Analyses

Parameters and variables of bioreactor performance

Gas flowrates were measured by acidified water displacement method (Escamilla-Alvarado et al. 2012). Biogas volumes and flowrates were standardized (273 K/101.18 kPa, Avogadro conditions). Concentrations of H_2 and CH_4 in bioreactors biogas were determined in a GOW-MAC-580 gas chromatograph equipped with a column packed with Molecular Sieve 5A and thermal conductivity detector as reported elsewhere (Robledo-Narváez et al. 2013).

The analysis of VFA (volatile fatty acids) was performed by gas chromatography in a Varian Star 3400 equipped with FID according to Muñoz-Páez et al. (2013). Prior to analysis, the effluents from the AnFBRs were centrifuged at 6000 rpm for 10 min, and the liquid was filtered through a 0.22-μm microfilter. The collected volume 1 mL was kept at − 4 °C until analysis.

COD, VSS, pH, and alkalinity were analyzed according to the Standard Methods (APHA-AWWA-WPCF 1985).

Reducing sugars, total phenolic compounds, and furfural were determined according to the techniques described in

previous works (Hernández-Correa et al. 2017; Miller 1959; Graham 1992; Ghanavati et al. 2015).

Characterization of bioparticles and embedded nanobioparticles by scanning electron microscopy coupled to energy-dispersive spectroscopy

Once the AnFBR-H and AnFBR-M exhibited a stabilized performance in hydrogen or methane production (15% H_2 and > 60% CH_4 contents in biogas, respectively), 10 g_{wb} samples of bioparticles were withdrawn from each bioreactor. Samples were dried under inert N_2 atmosphere and stored in serum bottles in anoxic conditions. Then, biofilms developed in AnFBR-H and AnFBR-M were observed in a Dual Beam FIB microscope.

For SEM analysis, the ENBP were analyzed with a field emission scanning electronic microscopy JEOL JJSM-7401F equipped with an EDS microprobe. The conditions were an accelerating voltage from 3 to 20 keV, with takeoff angle of 30° in a magnification range from 500 to 10,000.

Dynamic light scattering

The samples were dried under inert N_2 atmosphere. One milligram of pulverized sample was resuspended in 1 mL of deionized water. Afterwards, samples were sonicated for 40 min and immediately placed into a zeta sizer under the following conditions: angle 173 °C, refractive index 2.42, and an absorption index of 0.001 reported for magnetite (Lim et al. 2013).

High-resolution transmission electron microscopy

The ENBPs were analyzed by high-resolution transmission electron microscopy (HRTEM) using a JEOL Model JEM-2010 microscope equipped with an LaB6 cathode, at 200 keV and current of 102 μA (Ramírez-Nuñez et al. 2018). The samples were diluted in methanol and sonicated for 10 min. Once dispersed, the ENBP samples were placed on a copper grid mesh no. 200 for further analysis.

X-ray photoelectron spectroscopy

The surface of bionanoparticles was examined by XPS using a Thermo Scientific spectrophotometer equipped with a monochromatic Al K Alpha X-ray source and excitation line at 1487 eV. The samples were degassed previously under N_2 atmosphere for 24 h and then loaded in the analysis chamber at a pressure of 1×10^{-9} Torr (Pérez-González et al. 2018).

X-ray diffraction analyses

The diffraction pattern of the crystalline structure of ENBP was observed in a Bruker D8 Advance Eco diffractometer. The position angle 2θ varied from 5 to 100°, the step degree was 0.02°, and discrimination ranges from 0.18 to 0.25, with rotation of 10 rpm and copper source without monochromator. The X-ray structure was compared to reference crystallographic structure #998-002-0596 from de ICDD database.

Infrared spectroscopy

The ENBPs were pressed previously using KBr and examined in a FTIR Nicolet 6700 spectrometer. The transmittance was determined at room temperature in the interval 400–4000 cm^{-1}.

Specific surface area by Brunauer-Emmett-Teller adsorption method

The samples were dried under nitrogen atmosphere and degassed at 250 °C overnight and then were measured using a Gemini 2360 Surface Area Analyzer according to the instructions in the Operator's manual V5.01.

Results and discussion

Characteristics of hydrolysates

The efficiency in volume recovery of hydrolysate was 85%; the concentration of reducing sugars was 28 g L^{-1}. Regarding the toxicants, the average concentration of total phenolic compounds was 700 mg L^{-1}, whereas the average concentrations of furfural and 5-hydroxymethylfurfural were 690 and 2600 mg L^{-1}, respectively. At the end of the detoxification with PAC, the toxic compounds decreased at least by 90% and reducing sugar concentration remained close to 25 g L^{-1}. The detoxified hydrolysate was kept frozen and thawed before use for feeding bioreactors and the biogenic synthesis of ENBPs.

Performance of anaerobic fluidized bed reactors using hydrolysates from the organic fraction of municipal solid wastes

In general, the performance of AnFBR-H regarding bioH_2 production was poor to moderate. H_2 concentration in biogas was equal or less than 15% over time. At the end of S3 (stage 3), there was a slight increase in H_2 production, which could result from a greater proportion in the volume of hydrolysate, compared to the sucrose proportion added to the feed wastewater (Fig. S1, in the Supplementary Material document). In the early stages S1 and S2 when sucrose was the main carbon source, the low molecular weight metabolites were predominantly acetic, propionic, and butyric acid likewise ethanol (Table S1). When the feed was switched to 100% hydrolysates, VFA and ethanol concentrations significantly decreased, although lactic acid increased 18-fold.

It has been reported that under certain conditions the anaerobic metabolic pathways lead to ethanol production and acetate, which causes the reduction of theoretical hydrogen yield to 2 mol H_2/mol glucose (Eq. 2) (Ghimire et al. 2015).

$$C_6H_{12}O_6 + 2H_2O \rightarrow CH_3CH_2OH + CH_3COOH + 2CO_2 + 2H_2 \quad (2)$$

In our case, in the early stages of operation the AnFBR-H when the carbon source was sucrose, there was an outstanding accumulation of propionic acid (16 g L^{-1}, S1). This could be explained by the exceptional behavior of selected strains of *Clostridium*, i.e., *Clostridium articum*, that is a H_2 consumer (instead of H_2 producers, such as most known *Clostridium* strains) and produces propionic acid (Kumar et al. 2006). A decrease in VFA concentration was observed in S3, when AnFBR-H was fed with a greater volume proportion of hydrolysates (60%). In this case, the metabolic deviation favored the accumulation of lactic acid presumably by shifts in the composition of the anaerobic consortium, related to the presence of lactic acid bacteria (Eqs. 3a and 3b) (Muñoz-Páez et al. 2013).

$$C_6H_{12}O_6 \rightarrow 2CH_3CHOHCOOH \quad (3a)$$

$$C_6H_{12}O_6 \rightarrow CH_3CHOHCOOH + CH_3CH_2OH + CO_2 \quad (3b)$$

Low hydrogen production in AnFBR-H has been associated to the accumulation of lactic acid which is converted from glucose by species such as *Bacillus* spp. or by heterolactic fermentation from pentoses and hexoses by strains *Lactobacillus* spp. and *Lactobacillus oligofermentans* (Andreevskaya et al. 2016; Ghimire et al. 2015). Interestingly, several works on biological hydrogen production have observed that some strains of *Clostridium* can enhance hydrogen yields from lactic acid (Chojnacka et al. 2011; Hung et al. 2007; Sikora et al. 2013; Yang et al. 2007). This could explain that despite having a high cumulative concentration of lactic acid (≈ 5305 mg COD L^{-1}) in S5, our AnFBR-H was able to increase its bioH_2 production (Fig. S1).

On the other hand, AnFBR-M showed a more regular performance using either sucrose or hydrolysates as carbon sources (Fig. S1). Particularly at the start of S4 (day 60), there was a gradual increase of CH_4 production and relatively steady performance until the bioreactor received 100% of hydrolysates in its feed. At this time, CH_4 content in biogas reached 70 to 80% v/v.

The soluble metabolites in the effluent of AnFBR-M are presented in Table S1. It was found that once the feed wastewater was turned to a regime based in hydrolysates (S4), the average concentration in VFA decreased in an outstanding way, which was consistent with increased methane production (Fig. S1).

In the early stage S1, when AnFBR-M was fed with only sucrose, there was an increase in VFA concentration that could be due to an imbalance between acidogenic and methanogenic populations reflected in low methane production (Habouzit et al. 2014). In course of time, the decrease in the organic loading rate from 10 to 3.33 g L^{-1} day^{-1} possibly allowed for attaining an equilibrium of populations that later promoted a stable performance. A more robust methanogenic performance was observed in S5; there was a decrease in VFA concentration as well as enhanced methane production as it was mentioned above.

Characterization of embedded nanobioparticles

Results of the characterization of ENBP are presented in a summarized form in Table S2 (Supplementary Material document) following the scheme of the 2^2 factorial experiment.

SEM microscopic characteristics of ENBPs are presented in Fig. 1. Table 2 exhibits results of the specific surface area of ENBPs by BET analysis. The elemental composition of ENBPs by EDS is shown in Fig. 2, with emphasis on total iron. Figures 3, 4, 5, and 6 exhibit the HRTEM micrographs of the ENBPs. The XPS results that provide evidence of iron speciation are displayed in Fig. 7. Further evidence of size distribution and agglomeration of NP in the ENBPs using DLS is shown in Fig. 8. Structural patterns of the oxides found in the ENBPs were determined by XRD and collected in Table 3 and Fig. 9. More information on chemical composition of the ENBPs was obtained by IR and displayed in Fig. 10 as well as Tables S3, S4, S5, and S6 (Supplementary Material document). Finally, results of pH of biosynthesis media and COD removal efficiencies were reported in the text of this subsection.

Microscopic characteristics of bioparticles and embedded nanobioparticles

The bioparticles withdrawn from de AnFBR-H and ANFBR-M were observed by SEM in order to evaluate the colonization of the GAC. Figure 1 a and b indicate that biofilm coverage of the GAC particle was incomplete; this is also known as "patchy growth." Moreover, biomass growth on the BP withdrawn from the hydrogenogenic bioreactor was lower than that in the BP from the methanogenic bioreactor. This was possibly due to the selective pressures applied to the inoculum in the hydrogenogenic bioreactor (such as the heat shock pretreatment and the acidic regime), which could have limited the microbial diversity.

Presumably, it seems that there was some deposition of small mineral scales on BP of the hydrogenogenic bioreactor. Magnification of the micrographs was not sufficient to appreciate in detail the morphology of microbes that constituted the biofilms, although in Fig. 1b, it seems that there are some

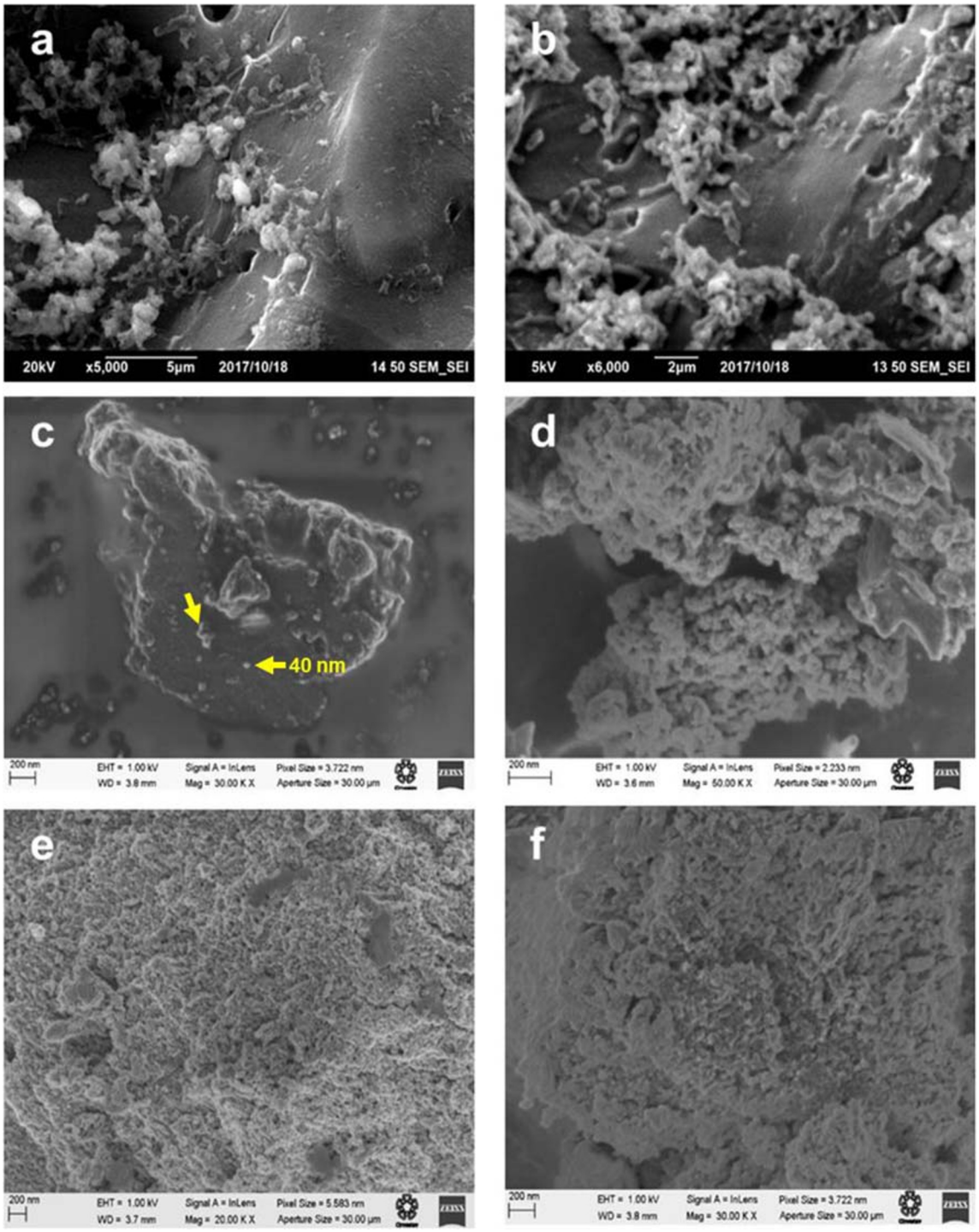

Fig. 1 Scanning electron microscopy micrographs of biofilms developed in 90 days of operation in **a** AnFBR-H, hydrogenogenic and **b** AnFBR-M, methanogenic bioreactors fed with hydrolysates from the organic fraction of municipal solid wastes. Different nanodecorated bioparticles synthesized from $FeCl_3$ 0.25 M and bioparticles from AnFBR-H (**c**) and AnFBR-M (**d**). Frames **e** and **f** correspond to nanodecorated bioparticles synthesized from ferric citrate 0.1 M using bioparticles from AnFBR-H and AnFBR-M, respectively

diplococcus-like and rod-like shapes. Several methanogenic archaea that can be found in methanogenic reactors devoted to waste treatment are typically short and long bacilli, cocci in several association patterns (sarcina), as well as filamentous shapes (Corrales et al. 2015).

Structures that resembled isolated NPs in the amorphous matrix of the ENBP were observed in frames c to f of Fig. 1. Regarding this, the asymmetric and unequal morphology of biomagnetite nanoparticles has been discussed; previous reviews have found that biomagnetite nanoparticles have

Table 2 Specific surface areas and Langmuir isotherms for nanoparticles in embedded nanobioparticles

Parameter	ENBP-H[a] 0.25 M $FeCl_3$	ENBP-M[b] 0.25 M $FeCl_3$ M	ENBP-H[a] 0.1 M Ferric citrate	ENBP-M[b] 0.1 M Ferric citrate
Langmuir (m^2 g^{-1})	914.34	892.35	699.33	914.16
BET 1-pt (m^2 g^{-1})	640.86	630.60	496.29	649.28
Total pore volume (cm^3 g^{-1})	0.40	0.39	0.29	0.38

The determination of the specific surface area was performed by triplicate

[a] Nanodecorated bioparticles originated in the hydrogenogenic bioreactor

[b] Nanodecorated bioparticles originated in the methanogenic bioreactor

amorphous distribution and size, in contrast with the chemical synthesized magnetite (Guo and Barnard 2013).

Analysis by EDS of nanoparticles embedded in the agglomerated material confirmed the presence of iron and oxygen in the mapped region and a size of approximately 40 nm for NP in the matrix (Fig. 1c).

Our results were close to those reported by Kim et al. (2015), where anaerobic bacteria biosynthesized siderite, akaganeite, and schwertmannite particles from acid mine drainage that contained iron oxyhydroxide at room temperature. Glucose was added as a source of reducing power (10 mM).

Specific surface area

On the other hand, according to BET analysis (Table 2), the specific surface area of the NP of our four ENBPs (480 to 625 m^2 g^{-1}) was superior to that reported in previous works for NP synthesized by co-precipitation method (286.9 m^2 g^{-1}; Ma et al. 2014). Iron oxide nanoparticles with a high specific surface area have been widely studied because of its physicochemical properties and potential applications in catalysts and adsorbents, for instance, in remediation of organochlorinated pollutants.

Furthermore, in previous studies, it was observed that small size of nanoparticles and high surface area play an important role in environmental processes, for instance, in mine tailing remediation as well as groundwater treatment (Kim et al. 2015).

Elemental composition of the embedded nanobioparticles analyzed by energy dispersive spectroscopy

The composition of iron ENBPs synthesized from 0.25 M $FeCl_3$ and hydrolysates was determined by EDS (Fig. 2); the values obtained for elemental composition in ENBP-H were O

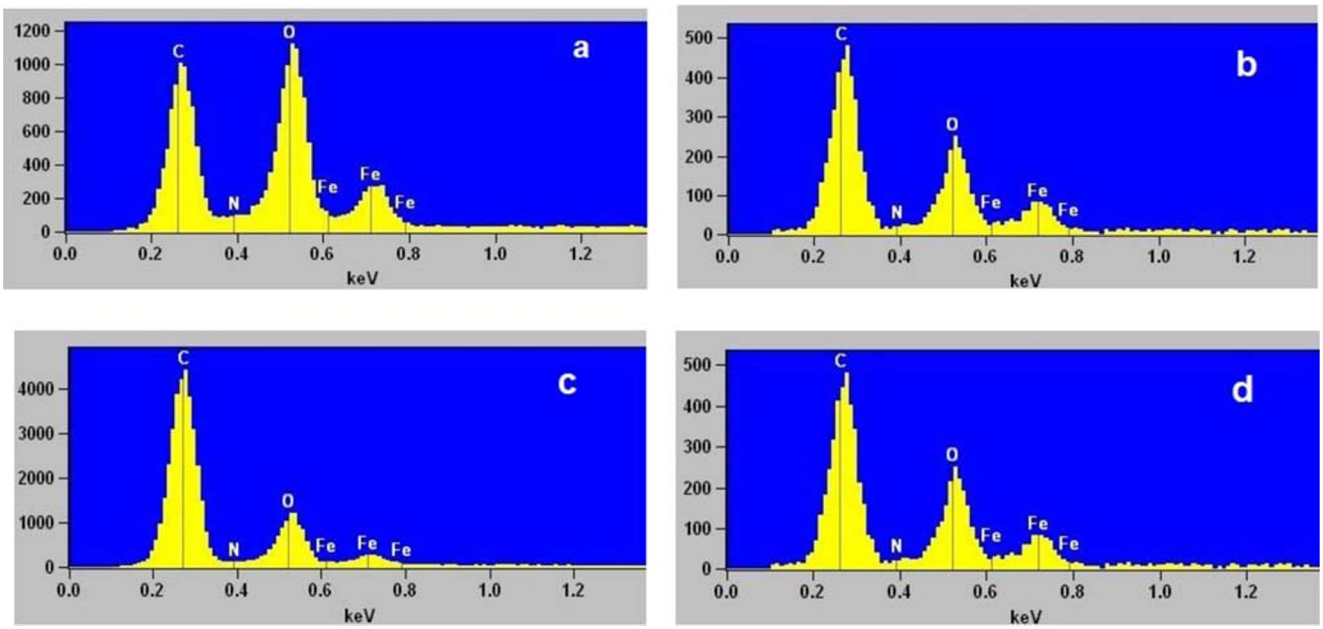

Fig. 2 Energy-dispersive spectroscopy (EDS) of several ENBPs **a** originated in the hydrogenogenic bioreactor and synthesized from 0.25 M $FeCl_3$ and hydrolysates (16 g L^{-1}), **b** originated in the methanogenic bioreactor and using 0.25 M $FeCl_3$ and hydrolysates (10 g L^{-1}), **c** originated in the hydrogenogenic bioreactor and synthesized from 0.1 M ferric citrate and hydrolysate (16 g L^{-1}), and **d** originated in the methanogenic bioreactor and using 0.1 M ferric and hydrolysate (10 g L^{-1})

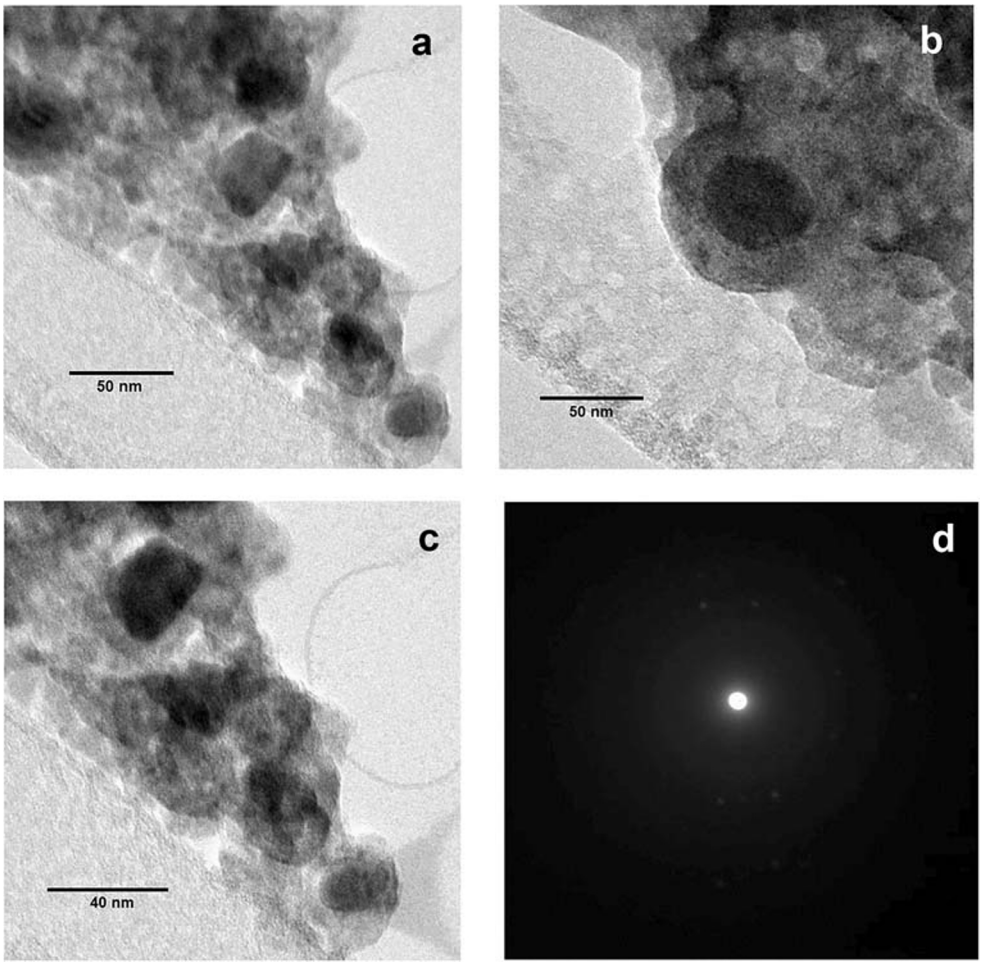

Fig. 3 Images of bionanoparticles ENBP-H $FeCl_3$ by HRTEM: **a**, **b** medium resolution, **c** high resolution, and **d** selected area electron diffraction pattern (SAED)

(35.36%) and Fe (64.64%); and for the ENBP-M, the composition was O (39.45%) and Fe (60.55%).

Regarding the synthesis of ENBP using ferric citrate 0.1 M as salt precursor, the results in composition analysis by EDS were ENBP-H, O (91.41%) and Fe (8.59%); in the case of ENBP-M, O (37.46) and Fe (62.54%) were found.

There was a strong interaction between both factors for the iron content response variable ($p < 0.05$) (in this scenario, it is recommended to disregard the main effects and concentrate in the interaction; Montgomery 2017) (Fig. S2): when the salt was $FeCl_3$, the Fe content slightly decreased from 64.64 to 60.55% for the ENBP-H and ENBP-M, respectively. When the synthesis was based on Fe citrate, the Fe content dramatically increased from a very low value 8.59% to a maximum of 62.54% for the ENBP-H and ENBP-M, respectively. Overall, Fe contents of nanoparticles in ENBP-M were less sensitive to the effect of the "type of iron salt." These results were somewhat unexpected. The statistical interaction outcome deserves more research and interpretation in terms of physical, chemical, and biological arguments. Also, we should be cautious because the iron content can be contributed not only by magnetite but also by other compounds such as siderite and di-iron trioxide (hematite).

Assessment of bionanoparticles by high-resolution electron microscopy

Table S2 in the Supplementary Material document summarizes the results of HRTEM as well as others for the four "treatments" in our work. From analysis of the bionanoparticles by HRTEM, it was observed a spherical shape and agglomeration, particularly for samples H and O synthesized from ferric chloride. Particle size was ~40 nm (Fig. 3a–c) which was consistent with findings by SEM mentioned before. The electron diffraction confirmed the crystallinity of the ENBP-H.

Regarding ENBP-M $FeCl_3$, bionanoparticles exhibited a spherical shape and a finer crystalline structure and particle size ~42 nm (Fig. 4a, b). High-resolution lattice image showed a heterogeneous structure that could be attributed to different orientations of crystals (Fig.4c). The diffracted electron pattern of ENBP-M $FeCl_3$ can be observed in Fig. 4d by SAED.

In case of ENBP-H citrate, the shape of crystals was hexagonal whereas size was ca. ~62 nm; there was a certain degree of agglomeration (Fig. 5a and b). The image of lattice in Fig. 5c showed a contrast in different zones in which dark

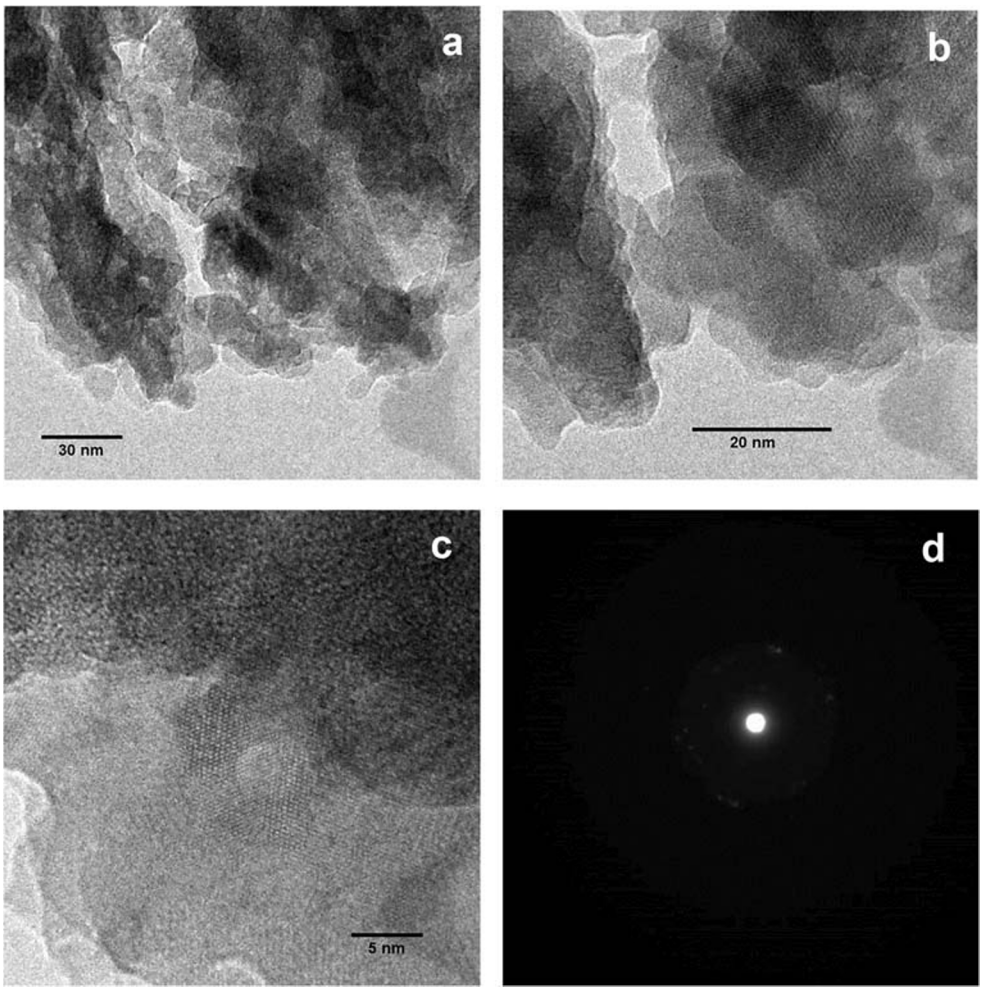

Fig. 4 Micrographs of bionanoparticles ENBP-M $FeCl_3$ analyzed by HRTEM: **a**, **b** medium resolution, **c** high resolution, and **d** image corresponding to SAED pattern

areas were attributed to organic matter, mainly in the form of carbon and precursors such as citrate. Also, in Fig. 5c, the same phenomenon of different crystallographic orientation was observed, possibly due to the presence of mixture of iron phases (as suggested by diffraction patterns by XRD; Fig. 9). Regarding the SAED pattern (Fig.5d), we found an increase in the presence of bright spots in the rings of diffracted electron.

Concerning ENBP-M citrate, the particles presented lower agglomeration, hexagonal shape, and size ~40 nm (Fig. 6). The lattice showed a more uniform orientation, and more fine crystalline structure was observed in SAED (Fig. 6d).

In the present work, according to SEM and HRTEM micrographs, the nanomaterial prepared from $FeCl_3$ exhibited characteristic clusters of agglomerated particles, size dimensions in a range from 40 nm, and spherical shape (Figs. 1c, 3, and 4).

Regarding our ENBP, the use of ferric citrate as iron precursor promoted greater crystallinity (according to SAED pattern) as well as changes in morphology since presenting hexagonal shape of particles (HRTEM) (Table S2; Figs. 5 and 6). The average size was ca. 40 and 60 nm for ENBP-M and ENBP-H citrate and presented different orientation shown in the lattice image by high resolution, particularly in ENBP-M citrate (Fig. 6).

Shape and size of EBNP synthesized with $FeCl_3$ in our work were consistent with previous research of Kastrinaki et al. (2018). In their experiments, the authors used two iron salts, Fe $(NO_3)_3$ and $FeCl_3$, in order to compare the effect of iron source on the morphology of the NP. According to their TEM results, spherical morphology was observed in both cases. Their NP presented cavities when synthesized from Fe $(NO_3)_3$ and in case of $FeCl_3$ NP, an additional oxide layer was formed. The authors discussed that these variations could be related to differences between water solubility of Fe $(NO_3)_3$ and $FeCl_3$, 150 mg mL^{-1} and 92 mg mL^{-1}, respectively. Higher solubility values for iron nitrate solution would have released more soluble ions, unlike ferric chloride. Thus, the spherical shape of Fe $(NO_3)_3$ NP resulted in homogeneous morphology, whereas in the opposite case, lower solubility of ferric chloride would lead to an amorphous surface.

In a work of synthesis of iron nanoparticles by extracts of *Mucuna pruriens* (a seed from Indonesia) and $FeCl_3$ (Sardjono et al. 2018), the main material formed was magnetite, whereas the NP shape was spherical and exhibited a

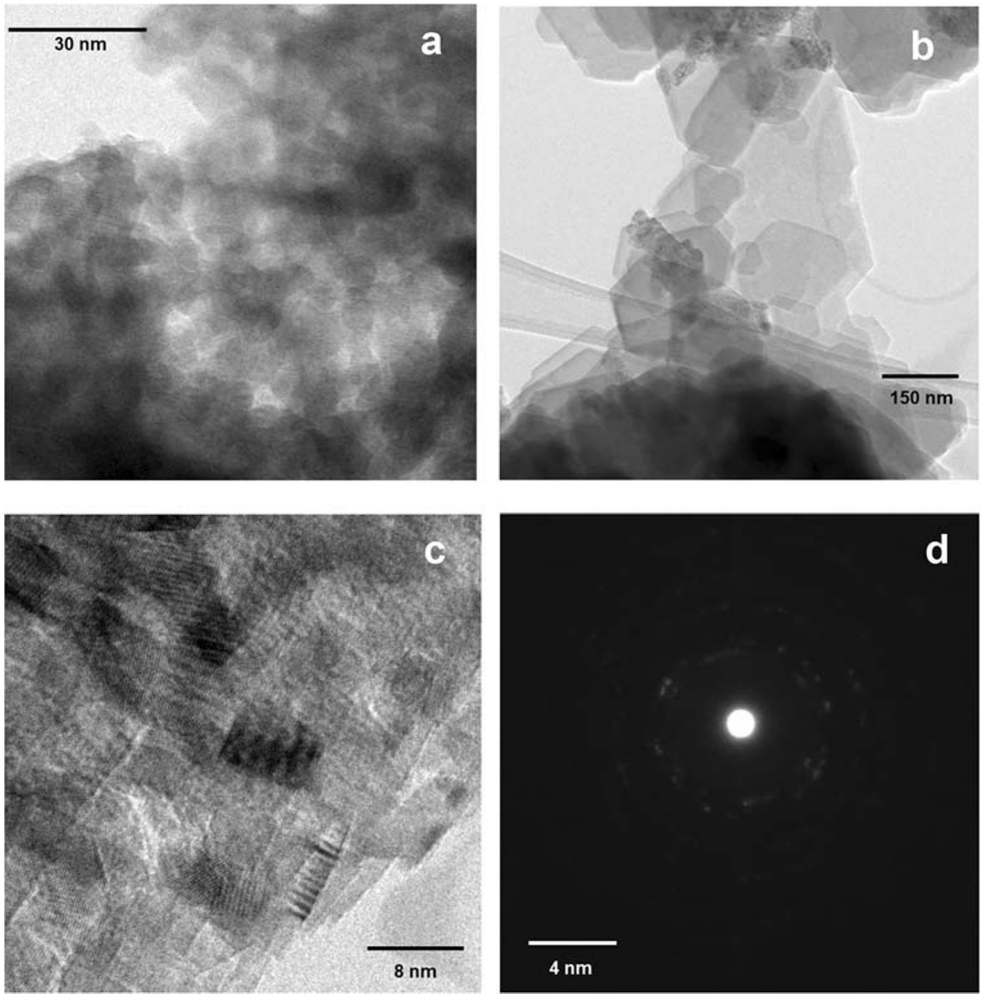

Fig. 5 Micrographs by HRTEM corresponding to ENBP-H Ferric citrate 0.1 M: **a**, **b** medium and lower resolutions, **c** image in high resolution of nanoparticle lattice showing the crystal orientation, and **d** SAED pattern

medium size (30 nm average). The NP were present as agglomerates.

Our results on crystallinity of the EBNP (Table S2) were in agreement with findings by Liu et al. (2017). They evaluated the effect of type of iron salts on crystallinity of the FeCo NP. They found higher crystallinity and more uniform distribution (better dispersion) in NP produced from ammonium iron citrate that in those prepared from iron nitrate salt. Using XRD analysis, the FeCo NP synthesized with ammonium iron citrate showed more crystalline domains (311, average FWHM value of 0.9°) than the NP samples prepared from iron nitrate solution (average 2.0° for the same peak). This effect was explained by the authors in terms of the formation of a complex ion from citrate and iron atoms and free oxygen in the hydroxyl and carboxyl group. According to the authors, this complex ion would have allowed the precipitation and greater dispersion of the NP.

X-ray photoelectron spectroscopy

The XPS spectra are shown in Fig. 7. Spectra were obtained with a constant energy step size of 1.0 eV; they can be used for organic and inorganic materials (Pérez-González et al. 2018). It should be noted that in the four ENBPs, two characteristic binding energies for iron oxides species at $2p_{3/2}$ for high bonding energies and $2p_{1/2}$ for lower energies were found, see Fig. 7a, c, g and e (and Fig. 9 for XRD pattern). According to literature, the binding energy for the spectra for Fe $2p_{1/2}$ was in the range of 717–725 eV (Kim and Park 2002).

In the case of Fe $2p_{3/2}$ for ENBP-M (using both salts, $FeCl_3$ and ferric citrate), the spectra presented more signals that could be possibly attributed to Fe^{III} tetrahedral (712–714 eV) or Fe^{III} octahedral (710–712 eV) (Fig. 7c and g).

According to our results in XRD analysis, the ENBPs presented a mixture of iron oxides phases. This was also suggested in the XPS spectra by the occurrence of multipeaks at several binding energies whose values were near to those of the characteristic iron oxides reported in literature such as Fe_3O_4 (magnetite), hematite (α-Fe_2O_3), and maghemite (γ-Fe_2O_3) (Poulin et al. 2010; Lesiak et al. 2019; Moulder et al. 1992).

It has been previously reported that in the Fe2p line spectrum from Fe_3O_4 (magnetite), the satellite is usually at 714 eV (Fujii et al. 1999). For α-Fe_2O_3 (hematite), the satellite peak

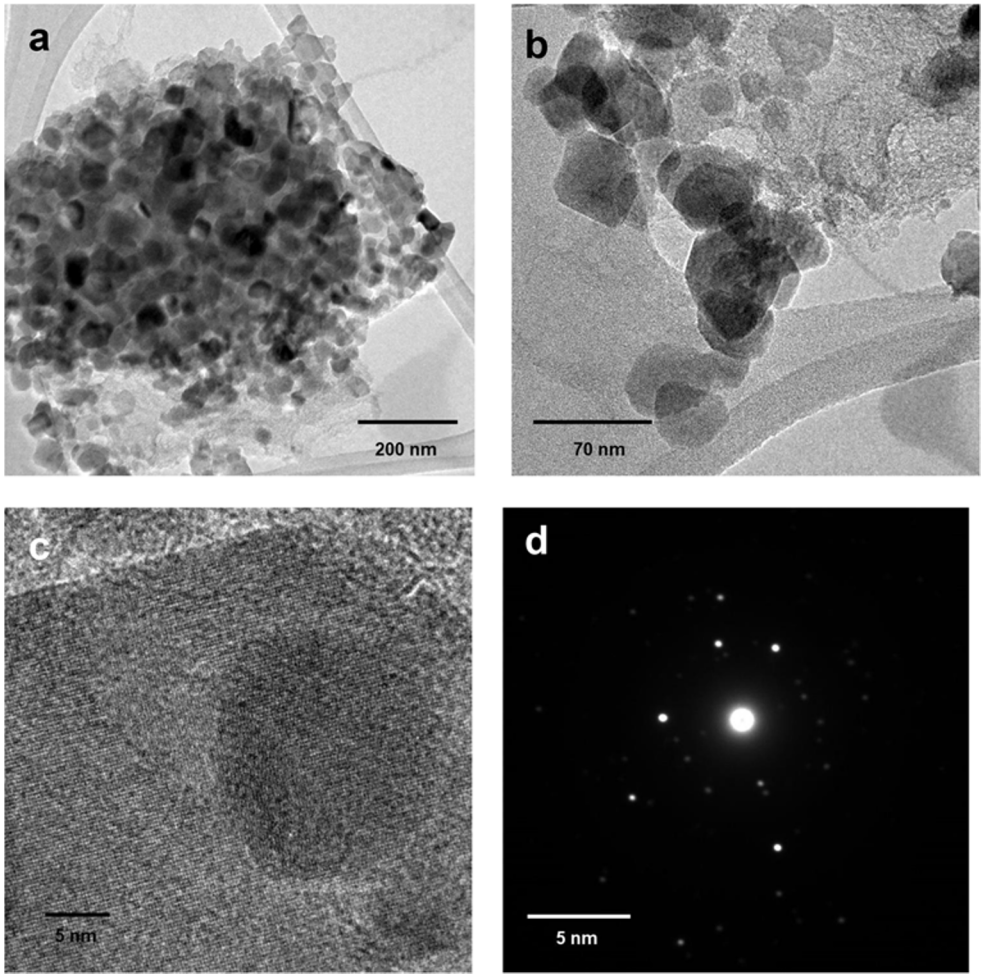

Fig. 6 Images of ENBP-M citrate analyzed by HRTEM: **a**, **b** low and medium magnifications, **c** micrography of lattice showing the crystal orientation, and **d** SAED pattern

appears approximately at 719 eV (Radu et al. 2017; Zhong et al. 2017). In our spectra, we found satellite peaks at 713.3 and 719.5 eV for Fe^{+2} and Fe^{+3}, respectively. Other satellite values were also found for Fe^{+2} in our samples (Table S2). This suggested the presence of magetite and hematite. Also, these findings were consistent with results obtained with XRD and IR (Table S2).

From the XPS analysis in the four ENBPs, there was a tendency to obtain characteristic peaks of 711 eV corresponding for hematite (α-Fe_2O_3) high spin Fe $2p_{3/2}$ and, for low spin $2p_{1/2}$, the binding energy was 724–725 eV.

Interestingly, it was found a slight effect of the precursor salt citrate or chloride on the peak intensities: values corresponding to nanomaterials synthesized with iron citrate were 4.9 to 6.5% higher than those of nanomaterials synthesized with iron chloride. Yet, this trend should be taken with caution because XPS determines the composition of the surface of the sample (Moulder et al. 1992; Zhong et al. 2017); the signals are thought to be more a qualitative indication than quantitative and also the small size of samples (Pérez-González et al. 2018).

In summary, XPS analysis showed the presence of both Fe(II) and Fe(III) in all the nanomaterials synthesized in our work. Satellite peaks revealed the likely presence of magnetite and hematite. These results agree with results obtained in this work using XRD and IR (Table S2; Figs. 9 and 10).

Size distribution of embedded nanobioparticles by dynamic light scattering

The size distribution in the ENBPs was also determined by DLS. It was observed that using 0.1 M ferric citrate as a salt precursor lead to smaller diameter of agglomerates than that obtained when using 0.25 M $FeCl_3$. Figure 8 shows that the average dispersion for the agglomerated ENBP were in the range from 600 to 1000 nm (frames a and b), for ENBP-H and ENBP-M synthesized from 0.25 M $FeCl_3$, whereas the average range of dispersion was much lower, in the range 400–700 nm (frames c and d) for ENBP-H and ENBP-M from ferric citrate. Thus, results from DLS confirmed the agglomeration found in some SEM and HRTEM micrographs of ENBP described before.

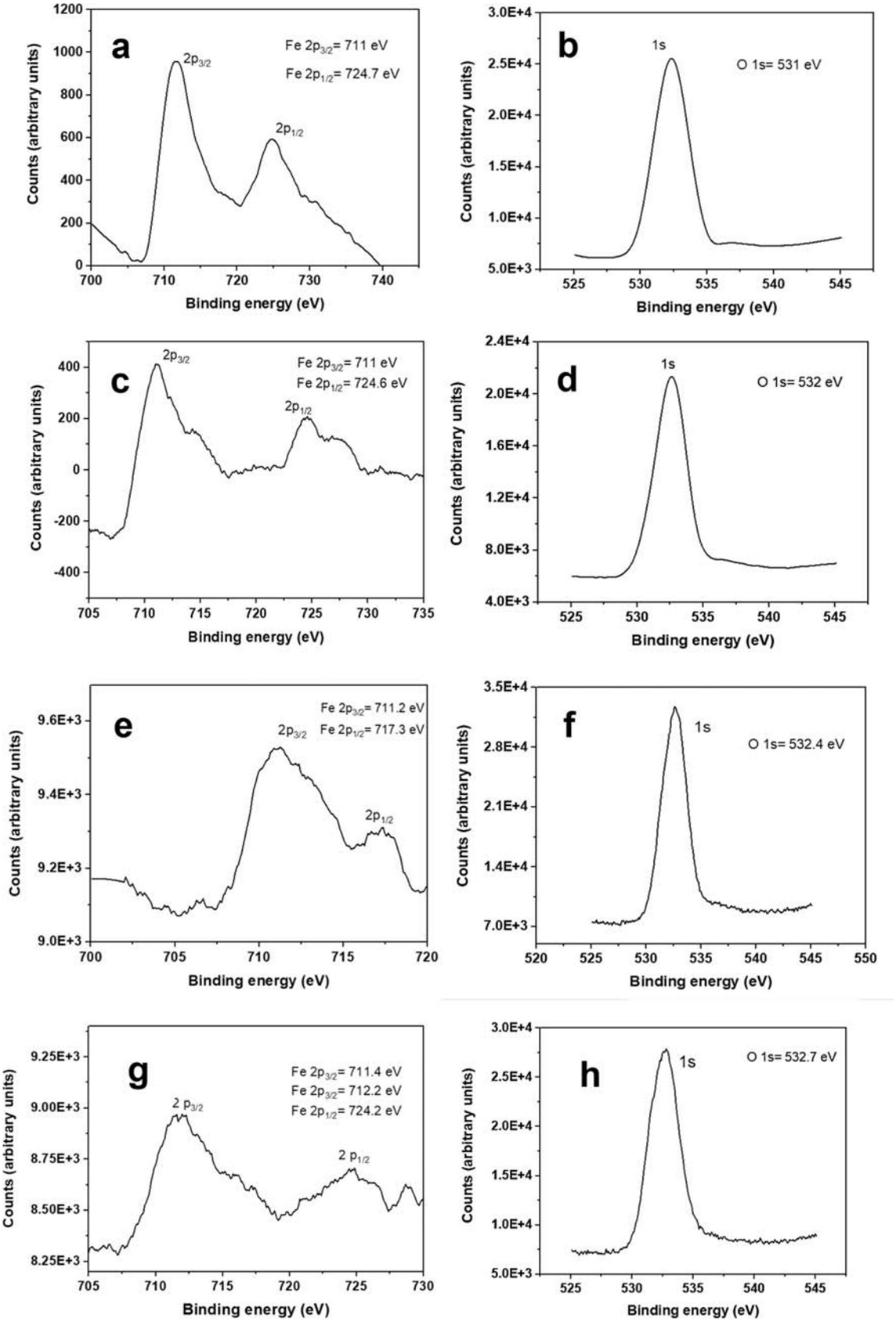

Fig. 7 Photoelectron spectra by XPS corresponding to Fe and O: **a**, b ENBP-H $FeCl_3$, **c**, **d** ENBP-M $FeCl_3$, **e**, **f** ENBP-H citrate, **g**, **h** ENBP-M citrate

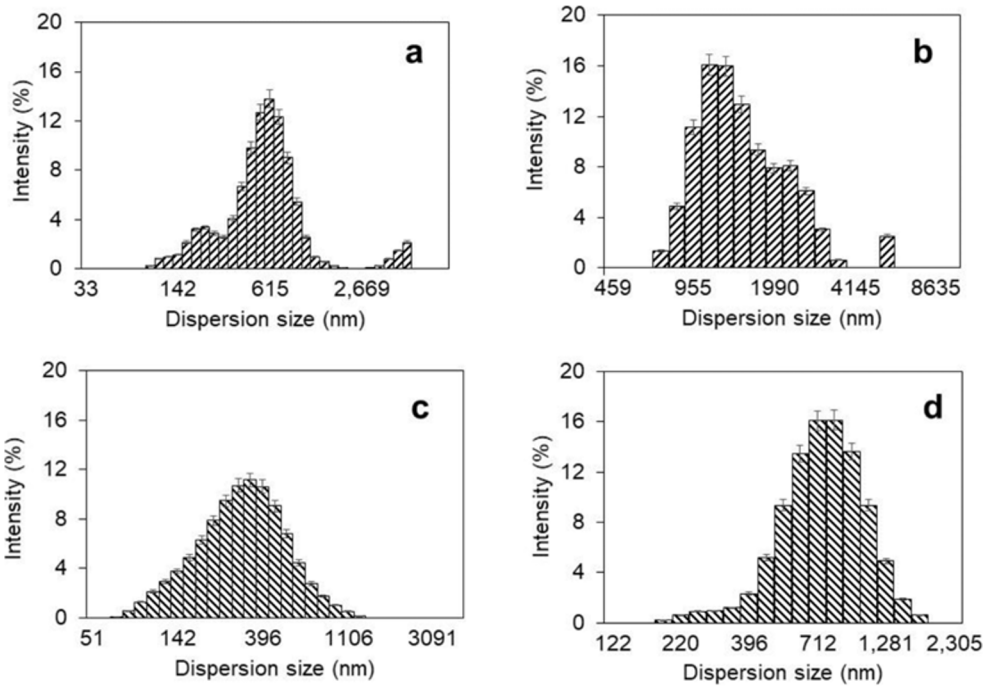

Fig. 8 Average dispersion of nanoparticles in ENBP analyzed by DLS (dynamic light scattering): **a** bioparticles from hydrogenogenic bioreactor and using 0.25 M $FeCl_3$, **b** bioparticles from the methanogenic bioreactor using 0.25 M $FeCl_3$, **c** bioparticles from hydrogenogenic bioreactor and using 0.1 M ferric citrate, and **d** bioparticles from the methanogenic bioreactor using 0.1 M ferric citrate

Structural pattern by X-ray diffraction studies

Table 3 shows the results obtained from the XRD patterns in the four different ENBPs. We obtained broad, relatively low relative intensity (RI) peaks (Fig. 9). The highest RI in were diffracted from the samples of ENBP synthesized with 0.1 M ferric citrate. Saranya et al. (2015) in a work about magnetite NP (Fe_3O_4) produced by hydrothermal method also reported very broad peaks that indicate a small crystallite size.

The diffraction patterns in the XRD analysis of ENBP showed a mixture of phases of iron oxides (Fig. 9; Table 3): magnetite (Fe_3O_4) (Anyika et al. 2017), siderite ($FeCO_3$) (Oza and Joshi 2017), and hematite α-Fe_2O_3 (Jaafarzadeh et al. 2017).

The following positions and planes were found in ENBP-H $FeCl_3$: magnetite Fe_3O_4 35° (3 1 1), 43° (4 0 0), and 62° (4 0 0), for siderite $FeCO_3$ 26° (0 1 2) and 38° (1 1 0), whereas for hematite α-Fe_2O_3 24° (0 1 2), 36° (1 1 0), and 50° (0 2 4).

On the other hand, in ENBP-M $FeCl_3$, the pattern diffraction showed the following phases and positions: magnetite Fe_3O_4 35° (3 1 1), 43° (4 0 0), and 62° (4 0 0); for siderite $FeCO_3$ 26° (0 1 2) and 38° (1 1 0); moreover, hematite was found at 24° (0 1 2), 36° (1 1 0), 41° (1 1 3), 50° (0 2 4), and 54° (1 1 6).

XRD analysis of ENBP-H citrate revealed magnetite Fe_3O_4 35° (3 1 1) and 62° (4 0 0) and siderite $FeCO_3$ 26° (0 1 2), 38° (1 1 0), and 42° (1 1 3). Regarding the hematite, the positions found were at 24° (0 1 2), 36° (1 1 0), 50° (0 2 4), and 54° (4 0 0).

In the samples of ENBP-M citrate, the angles and positions were the following: magnetite Fe_3O_4 35° (3 1 1), 43° (4 0 0), and 62° (4 0 0) and for siderite $FeCO_3$ 26° (0 1 2), 38° (1 1 0), and 42° (1 1 3). For hematite α-Fe_2O_3, the positions were at 24° (0 1 2), 36° (1 1 0), 50° (0 2 4), and 54° (4 0 0).]

Table 3 Planes and positions for the embedded nanobioparticles in our work from X-ray diffraction analysis

Sample	Magnetite Fe_3O_4	Siderite $FeCO_3$	Hematite α-Fe_2O_3
ENBP-H $FeCl_3$	35° (3 1 1) 43° (4 0 0) 62° (4 0 0)	26° (0 1 2) 38° (1 1 0) 42° (1 1 3)	24° (0 1 2) 36° (1 1 0) 50° (0 2 4)
ENBP-M $FeCl_3$	35° (3 1 1) 43° (4 0 0) 62° (4 0 0)	26° (0 1 2) 38° (1 1 0)	24° (0 1 2) 36° (1 1 0) 41° (1 1 3) 50° (0 2 4)
ENBP-H citrate	35° (3 1 1) 43° (4 0 0) 62° (4 0 0)	26° (0 1 2) 38° (1 1 0) 42° (1 1 3)	24° (0 1 2) 36° (1 1 0) 50° (0 2 4)
ENBP-M citrate	35° (3 1 1) 43° (4 0 0) 62° (4 0 0)	26° (0 1 2) 38° (1 1 0) 42° (1 1 3)	24° (0 1 2) 36° (1 1 0) 50° (0 2 4)

Analysis by infrared spectroscopy

Infrared spectra allowed to identify vibrational modes for magnetite (Fe_3O_4) and siderite in three of the ENBPs (Fig. 10a, b, and d). Regarding ENBP-H citrate (Fig. 10c), the peak for magnetite was not found; however, it was observed a signal for siderite (780 cm^{-1}).

Concerning the potential application of the ENBP of this work, there is a wide research about dehalogenation of organochlorinated compounds by magnetite nanoparticles, as well as positive evidence concerning the involvement of siderite and hematite, which will be discussed below. In general, the IR results were consistent with XRD and XPS analysis (Fig. 9; Tables S3, S4, S5, and S6), which reinforces the evidence found in this work.

In samples of ENBP-H $FeCl_3$, the typical vibrational modes for magnetite were observed at 565, 667, and 684 cm^{-1} (Fig. 10a; Table S3) (Ramírez-Nuñez et al. 2018; Saranya et al. 2015; Yadav 2018). Peaks attributed to siderite ($FeCO_3$) at 776 cm^{-1} (Santillán and Williams 2004) and hematite (α-Fe_2O_3) were detected at 465 and 477 cm^{-1} (Fig. 10a; Table S3) (Ristic et al. 2017; Li et al. 2012).

Magnetite Fe_3O_4 is recognized to be a conducting mineral that fosters the electron transfer in microbial species and is involved in dechlorination of toxic organochlorinated compounds. In a recent work, Leitao et al. (2018) evaluated the effect of the addition of magnetite nanoparticles (Fe_3O_4) when studying the dehalogenation of 1,2-dichloroethane (1,2-DCA). They reported that dechlorination rate increased 3.3 times when Fe_3O_4 nanoparticles were added to the dehalogenating mix culture, mostly composed by *Dehalococcoides mccartyi*. The final removal rate of 1,2-DCA in the treatment containing magnetite was 2.3 $\mu eq\ L^{-1}\ day^{-1}$, whereas in the experiment with no addition of nanoparticles, it was only 0.7 $\mu eq\ L^{-1} day^{-1}$.

It is interesting to remark that siderite $FeCO_3$ is a mineral generated from metal iron by oxidation in the presence of HCO_3^-, and it is naturally found in groundwater and saline groundwater (Xin et al. 2018), although it can be formed in nanosynthesis processes. Moreover, there is some evidence that siderite could be related to dehalogenation of selected organochlorinated compounds, according to Wu et al. (2014). They examined the remediation of saline waters contaminated with 1,1,1-TCA (1,1,1-trichloroethane) using zero valent iron nanoparticles (nZVI). They found that degradation efficiencies reached a maximum at higher concentrations of bicarbonate (100 mM) in the first 6 h.

Xin et al. (2018) studied the removal of trichloroethylene (TCE) by varying the composition of mineral salts and TCE concentration in the feedwater. Precipitated minerals produced in the experiments containing nZVI and HCO_3^- were analyzed by XRD, and the diffraction pattern for siderite ($FeCO_3$) was identified. In that case, the best efficiency for TCE removal was 99.6%.

There is also some evidence on the dehalogenating potential of hematite α-Fe_2O_3 on 2,4-dichlorophenoxy-acetic acid (2,4-D) (Jaafarzadeh et al. 2017). Nearly 30% removal of 2,4-D was obtained by using hematite NPs with the help of a redox mediator peroxymonosulfate. It seems that hematite NPs activated the peroxymonosulfate and the latter effected the dechlorination of 2,4-D. These results should be interpreted with caution because the experiment suggests that hematite NPs acted indirectly on the dechlorination of 2,4-D.

Choi et al. (2014) described the use of bimetallic NP Ni-Pd + hematite in experiments that allowed significant removal of perchloroethylene (PCE) (75% in 6 h) in batch tests initially loaded at 300 mM of PCE. On the other, the control without NPs exhibited a 5% removal efficiency.

In our work, the IR analysis of ENBP-M $FeCl_3$ showed the vibrational mode signal for magnetite at 563 and 667 cm^{-1} and $FeCO_3$ at 760, 825, and 1435 cm^{-1} (Fig. 10b).

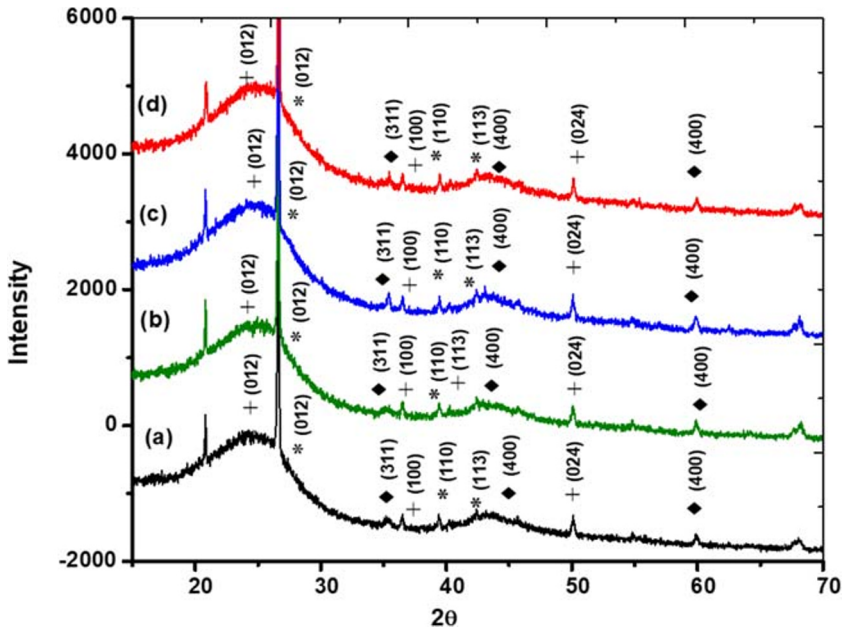

Fig. 9 X-ray diffraction plots corresponding to magnetite, siderite, and hematite present in ENBPs from hydrogenogenic and methanogenic bioreactors, synthesized using either 0.25 ferric chloride or 0.1 M ferric citrate

Additionally, a typical band for hematite α-Fe_2O_3 at 460 cm^{-1} was observed.

Regarding NP in ENBP-H citrate, weak bands for siderite (780 cm^{-1}) and for hematite (466 cm^{-1}) (Fig. 10c) were found.

In the case of ENBP-M citrate, the signals for magnetite were at 532, 559, and 629 cm^{-1}. Also, the vibrational modes for siderite were found at 1110 and 1420 cm^{-1}; moreover, the corresponding peaks for hematite were detected at 459 and 473 cm^{-1} (Fig. 10d).

Concerning changes in media pH after biosynthesis of NPs, a tendency to the acidification of the spent liquors was observed. In short, pH values in the "treatments" are mentioned below (where subscript i stands for initial, subscript f means final): ENBP-H $FeCl_3$ 0.25 M (pH_i 5.55, pH_f 4.61), ENBP-M $FeCl_3$ 0.25 M (pH_i 8.28, pH_f 6.89), ENBP-H Ferric citrate 0.1 M (pH_i 5.74, pH_f 4.87) and ENBP-M Ferric citrate 0.1 M (pH_i 8.22, pH_f 6.56).

Differences between initial pH of H and M synthesis are related to the pH required for dark fermentation H that has been reported to be between 4.5 and 5.8, whereas the typical pH of methanogenic bioreactors is from neutral to slightly alkaline (Estrada-Vázquez et al. 2003; Garibay-Orijel et al. 2005; Escamilla-Alvarado et al. 2013; Muñoz-Páez et al. 2013; Sotelo-Navarro et al. 2017).

Differences between pH_f of H and M treatments (pH_f of M > pH_f of H) can be explained in terms of two issues: M treatments not only started at higher pH_i than H ones, but also the buffering was higher (due to presence of bicarbonates and carbonates a pH 8.2; Ripley et al. 1986; Poggi-Varaldo and Oleszkiewicz 1992) than the buffer in the H vials. Therefore, final pHs in liquors of M biosynthesis are expected to be higher. Trends in final pH related to the type of precursor salt used were not so clear.

In our experiment, the association of vial pH and size of the ENBP (Table S2) corresponded strictly to a statistical

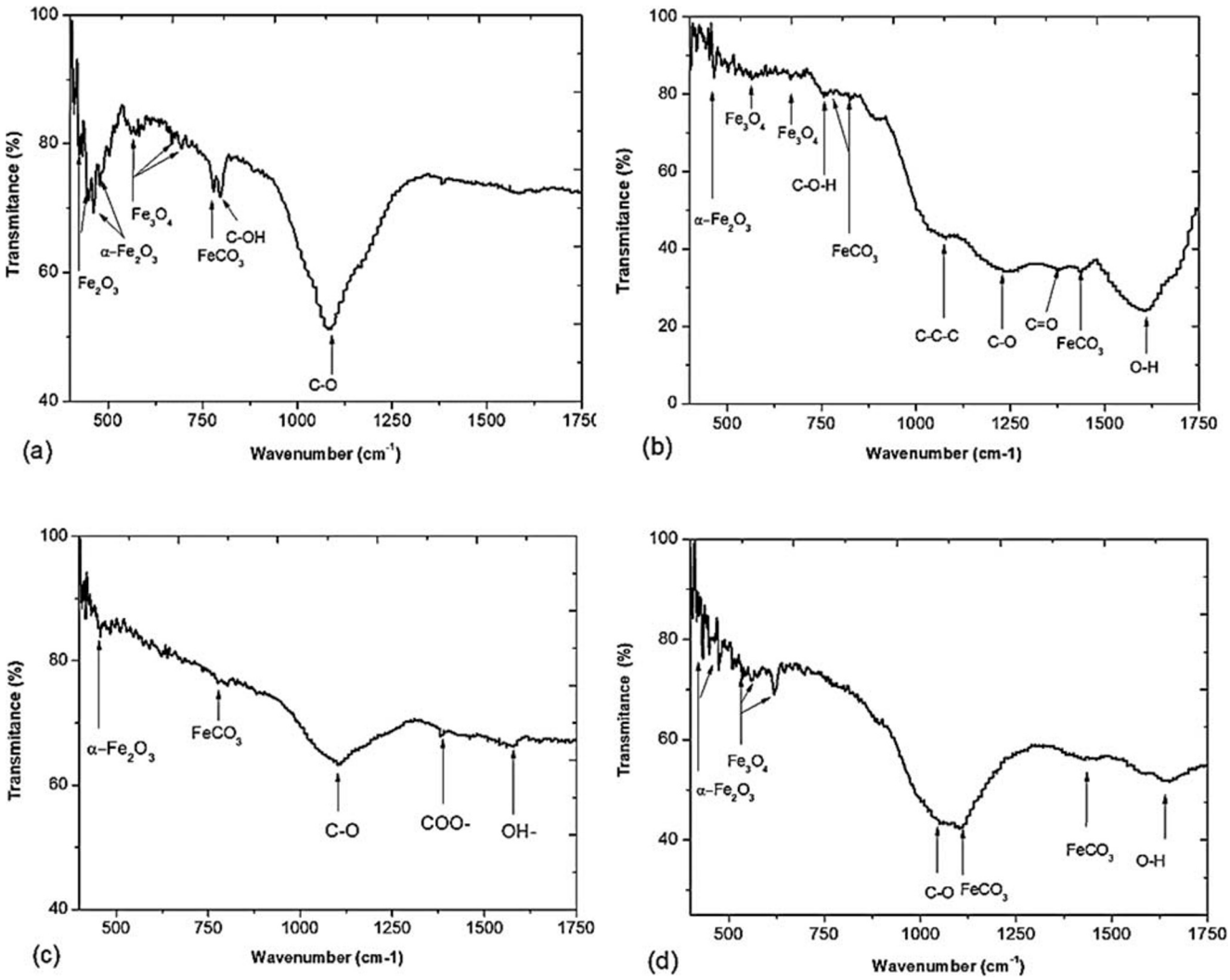

Fig. 10 Infrared spectra for embedded nanobioparticles (ENBP): **a** ENBP-H and **b** ENBP-M, both synthesized with 0.25 M $FeCl_3$; **c** ENBP-H and **d** ENBP-M, both produced from ferric citrate as salt precursor

interaction. Lowest sizes of NPs corresponded in general to the treatments EBNP-M (average size ca. 40 nm, independently of the type of precursor salt). Both treatments exhibited pH_f around 6.6–6.8. Yet, size of the EBNP-H at low pH (ca. 4.6–4.9 pH_f) had a divergent pattern depending upon the precursor salt: the one with $FeCl_3$ also displayed an average size of ca. 40 nm, whereas the one with iron citrate exhibited an average size near to 60 nm.

Previous works about microbial nanosynthesis of iron NPs such as magnetite (Fe_3O_4) have presented evidence regarding influence of pH on controlling the size of nanoparticles. For instance, when pH increased from neutral values to slightly alkaline values, NP size decreased. Kim and Roh (2018) examined a culture of indigenous Iron reducing bacteria that contained *Clostridium* strains and akaganeite as a magnetite precursor. They observed a quick shift in color of media and formation of the magnetic phase at pH of 8.5 and reduction of the size of nanoparticles in alkaline conditions (5–10 nm), whereas for pH 7.5 and 6.5, the values were slightly larger (5–25 nm and 15 nm, respectively). Regarding influence of pH on the shape of nanocrystals, the authors could not find significant differences since in all ranges of pH, the nanoparticles were principally spherical.

The effects of pH, $FeCl_3$, and temperature on the production of iron oxide nanoparticles synthesized by *Penicillium waksmanii* were analyzed by Honary et al. (2015). In that study, they found an inverse relationship between the pH and the dimensions of nanoparticles, since the size decreased from 131 to 77 nm when increasing values of the pH (7.0) in the medium.

Therefore, our results regarding the influence of pH on NP size generally agreed with trends presented in the open literature.

The COD (chemical oxygen demand) values were determined at the initial and final time of the bionanoparticle synthesis. The results were the following: ENBP-H $FeCl_3$ 0.25 M (COD_i 17,920 mg O_2 L^{-1}; COD_f 7424 mg O_2 L^{-1}), ENBP-M $FeCl_3$ (COD_i 10, 880 mg O_2 L^{-1}; COD_f 3328 mg O_2 L^{-1}), ENBP-H citrate (COD_i 17,600 mg O_2 L^{-1}; CODf 10,880 mg O_2 L^{-1}), and ENBP-M citrate (COD_i 9984 mg O_2 L^{-1}; COD_f 5376 mg O_2 L^{-1}). Consequently, the COD removal efficiencies (η_{COD}) were (in descending order) as follows:

$$69.44\%(\text{ENBPM-FeCl}_3) > 51.46\%(\text{ENBP-M Citrate}) > > 41.58\%(\text{ENBP-H FeCl}_3) > 34.62\%(\text{ENBP-H Citrate}) \quad (4)$$

Standard deviations of η_{COD} were $\leq 5\%$.

First, the effect type of salt precursor indicated a main effect on η_{COD} of 55.51 and 43.04% for $FeCl_3$ and iron citrate, respectively (pooling the sources of the ENBPs).

On the other hand, the effect of source of ENPBs on η_{COD} resulted in 60.45 and 38.10% for M and H, respectively (pooling the types of precursor salt).

From these trends, it could be inferred that there could be a higher bioreduction power in methanogenic environments used for the synthesis of ENBP-M (either $FeCl_3$ or ferric citrate precursor salt) due to more efficient consumption of organic matter and its transformation to reduced methane, as compared to dark fermentation processes (H). Thus, it could be hypothesized that this effect could influence selected properties of the ENBPs. For instance, our results indicated that there was a higher degree of crystallinity and dispersion in ENBP-M than that in ENBP-H (Figs. 4, 6, and 8; Table S2 in the Supplementary Material document). According to the XRD patterns, XPS analyses, and HRTEM results, the ENBP-M presented higher number of iron oxides phases, and the signals in their spectra were stronger (Figs. 9 and 10). The latter was in agreement with data obtained by EDS analysis, where the concentration of iron in two types of ENBP-M was consistently high (60–65%), whereas in ENBP-H, there was a variation in iron concentration that included low values (8.5–62%) (Fig. 2; Table S2).

Also, it is likely that the η_{COD} could have also been associated to the smaller size of the ENBP-M, in addition to the possible influence of pH that was discussed above. Whether one or the other (η_{COD} or pH) could have contributed more to the size of the ENBP cannot be determined with the current experimental information in our work.

An analysis that takes into account the η_{COD} in terms of precursor salt shows that biosynthesis performed with $FeCl_3$ exhibited higher η_{COD} than that with Fe citrate as it was mentioned above (Table S2). It seems that the type of precursor salt with the associated effect on η_{COD} might have influenced (or be associated with) the NP shape, crystallinity, and dispersion (Table S2). For instance, ENBPs synthesized with Fe citrate showed hexagonal shape (Figs. 5 and 6) (whereas the ones synthesized with $FeCl_3$ were spherical; Figs. 3 and 4), exhibited a higher degree of crystallinity, and were more disperse than those synthesized with $FeCl_3$.

So, the important issues are that we can associate a probable positive effect of η_{COD} on selected characteristics of ENBPs. This, in turn, could be related to the biological process that dominated the biosynthesis (H or M). On the other hand, it seems that the type of precursor salt used in the biosynthesis of ENBPs might have been related to another set of ENBPs features, such as crystallinity, shape, and agglomeration.

So far, in our research, we were able to implement a biological synthesis procedure for producing ENBPs using biocatalysts from bioreactors of a waste-based biorefinery as well as a hydrolysate of OFMSW. Characteristics of these nanomaterials seemed to be very attractive for possible application on remediation of wastewaters, groundwater, and soil,

due to their high specific surface area, the presence of iron nanomaterials such as magnetite and siderite that have been reported to be successful for degradation of organochlorinated compounds, and the bioreductive power likely associated to the significant organic matter removal η_{COD} during the biosynthesis stage.

Conclusion

Bioparticles from biological fluidized bed reactors from a biorefinery of OFMSW (that produces hydrolysates rich in reducing sugars) were nanodecorated by biological reduction of iron salts (ENBP). Factor origin of bioparticles (either from hydrogenogenic or methanogenic fluidized bed reactor) and "type of iron precursor salt" (iron chloride or iron citrate) were explored. X-ray diffraction patterns of ENBP showed the typical peaks for magnetite at 35° (3 1 1), 43° (4 0 0), and 62° (4 0 0); moreover, siderite diffraction pattern was found at 26° (0 1 2), 38° (1 1 0), and 42° (1 1 3). SEM and HRTEM showed amorphous distribution of NP on the bioparticles surface, although small structures that are nanoparticle-like could be seen in the SEM micrographs. Some agglomeration of NPs was confirmed by DLS. Average NP size was lower in general for NP in ENBP-M than ENBP-H according to HRTEM. The factors did not have a significant influence on the specific surface of NPs, which was high and in the range of 490 to 650 $m^2\ g^{-1}$.

Analysis by EDS displayed consistent iron concentration 60–65% iron in nanoparticles present in ENBP-M (bioparticles previously grown in methanogenic bioreactor), whereas the iron concentration in NPs present in ENBP-H (bioparticles previously grown in methanogenic bioreactor) was more variable in a range from 8.5 to 62%, depending on the iron salt. These results are known as statistical interaction, so no main effects of the factors could be drawn.

Results of infrared analysis of ENBP in our work were congruent with the presence of magnetite and occasionally siderite determined by XRD analysis as well as the presence of both Fe^{+2} and F^{+3} (and selected satellite peaks) observed by XPS.

Our results on the ENBPs seemed to be attractive, since iron NPs are known to be useful materials for wastewater remediation of several contaminants, such as the removal of chlorinated organic compounds. Finally, the biosynthesis of ENBP from waste hydrolysates could become a sustainable platform for such nanomaterials as well as an additional source of revenues for a waste-based biorefinery.

Acknowledgments The authors wish to gratefully recognize the Associate Editor and anonymous Reviewers for their advice and insightful comments. The authors wish to thank Mr. Rafael Hernández-Vera, M.Sc. (Environmental Biotechnology and Renewable Energies Group GBAER); Mr. Adolfo Tavira Fuentes, M. Sc. and Mr. Miguel Galvan Arellano, M.Sc. (both with SEES, Dept. Electrical Engineering); Dr. Álvaro Ángeles Pascual (LANE); Dr. Marcela Guerrero Cruz, Dr. Jaime Santoyo Salazar, Dr. Ángel Guillén Cervantes and Dr. Sergio Armando Tomás Velázquez (Dept. of Physics); Mr. Gabriel Marcelino Pérez, Cand. Dr. Sc. (Nanoscience and Nanotechnology Program); Prof. Elvira Ríos-Leal (Analytical Center of the Dept. of Biotechnology and Bioengineering); and Ms. Miriam Marisol Tellez Cruz, C and. Dr. Sc. (Dept. of Chemistry) from CINVESTAV-IPN, for their valuable advice and excellent technical assistance in operation and characterization of bioreactor performance as well as the characterization of bionanoparticles.

Funding information CINVESTAV-IPN provided partial financial support to this research. HMP-V also financially supported this research. CONACYT awarded a graduate scholarship No. 300205 to LRC and an Infrastructure Project to HMP-V.

References

Albergaria JT, Alvim-Ferraz MCM, Delerue-Matos MCF (2010) Estimation of pollutant partition in sandy soils with different water contents. Environ Monit Assess 171:171–180

Andreevskaya M, Johansson P, Jääskeläinen E, Rämö T, Ritari J, Paulin L, Björkroth J, Auvinen P (2016) Lactobacillus oligofermentans glucose, ribose and xylose transcriptomes show higher similarity between glucose and xylose catabolism-induced responses in the early exponential growth phase. BMC Genomics 17:539

Anyika C, Asri NAM, Majid ZA, Yahya A, Jaafar J (2017) Synthesis and characterization of magnetic activated carbon developed from palm kernel shells. Nanotechnol Environ Eng 2:16–41

APHA-AWWA-WPCF (1985) Standard methods for the examination of water and wastewater, 17th edn. American public health association, Washington DC

Bharde A, Rautaray D, Bansal V, Ahmad A, Sarkar I, Yusuf SM, Sanyal M, Sastry M (2006) Extracellular biosynthesis of magnetite using fungi. Small 2:135–141

Bretón-Deval LM, Poggi-Varaldo HM (2017) Chapter 12.2 Sustainable iron based bionano-bioparticles from a dehalogenating microbial consortium allows remediation of water polluted with PCE. In: Candal R, Curutchet G, Domínguez-Montero L, Macarie H, Poggi-Varaldo HM, Sastre I, Vázquez S (eds) Environmental Biotechnology and Engineering ISEBE Advances 2016 ISBN 978-607-9023-51-5. Publisher Cinvestav Mexico City, Mexico, pp 1007–1014

Bretón-Deval LM, Rossetti S, Ríos-Leal E, Matturro B, Poggi-Varaldo HM (2016) Effect of coupling zero-valent iron side filters on the performance of bioreactors fed with a high concentration of perchloroethylene. J Environ Eng:142. https://doi.org/10.1061/(ASCE)EE.1943-78700001093

Bretón-Deval L, Solorza-Feria O, Ríos-Leal E, Poggi-Varaldo HM (2013) Dechlorination of PCE with nanoscale particles of zero-valent iron and palladium. C-41. In: Sirabian RR and Darlington R (Chairs), Bioremediation and sustainable environmental technologies—2013. Second International Symposium on Bioremediation and Sustainable Environmental Technologies (Jacksonville, FL; June 10–13, 2013). ISBN 978-0-9819730-7-4, Battelle Memorial Institute, Columbus, OH. www.battelle.org/biosymp

Byrne JM, Muhamadali H, Coker VS, Cooper J, Lloyd JR (2015) Scale-up of the production of highly reactive biogenic magnetite

nanoparticles using Geobacter sulfurreducens. JR Soc Interfaces 107. https://doi.org/10.1098/rsif.2015.0240

Chen SS, Huang YC, Lin JY, Lin MH (2014) Dechlorination of tetrachloroethylene in water using stabilized nanoscale iron and palladized iron particles. Desalin Water Treat 52:702–711

Chieffi G, Giordano C, Antonietti M, Esposito D (2014) FeNi nanoparticles with carbon armor as sustainable hydrogenation catalysts: towards biorefineries. J Mater Chem A 2:11591–11596

Choi K, Lee N, Lee W (2014) Reductive dechlorination of tetrachloroethylene by bimetallic catalysts on hematite in the presence of hydrogen gas. Adv Environ Res 2:151–162

Chojnacka A, Blaszczyk MK, Szczesny P, Nowak K, Suminska M, Tomczyk-Zak K, Zielenkiewicz U, Sikora A (2011) Comparative analysis of hydrogen-producing bacterial biofilms and granular sludge formed in continuous cultures of fermentative bacteria. Bioresour Technol 102:10057–10064

Corr SA, Byrne SJ, Tekoriute R, Meledandri CJ, Broughman DF, Lynch M, Kerskens C, O'Dwyer L, Gun'ko YK (2008) Linear assemblies of magnetic nanoparticles as MRI contrast agents. J Am Chem Soc 130:4214–4215

Corrales LC, Antolinez-Romero DM, Bohórquez-Macías JA, Corredor-Vargas AM (2015) Anaerobic bacteria: processes they perform and their contribution to life sustainability on the planet. NOVA 13(23): 55–81

Escamilla-Alvarado C, Ríos-Leal E, Ponce-Noyola MT, Poggi-Varaldo HM (2012) Gas biofuels from solid substrate hydrogenogenic–methanogenic fermentation of the organic fraction of municipal solid waste. Process Biochem 47:1572–1587

Escamilla-Alvarado C, Ponce-Noyola T, Ríos-Leal E, Poggi-Varaldo HM (2013) A multivariable evaluation of biohydrogen production by solid substrate fermentation of organic municipal solid wastes in semi-continuous batch operation. Int J Hydrogen Energ 38:I2527–I2538

Escamilla-Alvarado C, Poggi-Varaldo HM, Ponce-Noyola MT (2017) Bioenergy and bioproducts from municipal organic waste as alternative to landfilling: a comparative life cycle assessment with prospective application to Mexico. Environ Sci Pollut Res 24:25602–25617

Estrada-Vázquez C, Macarie H, Kato MT, Rodríguez-Vázquez R, Esparza-García F, Poggi-Varaldo HM (2003) The effect of the supplementation with a primary carbon source on the resistance to oxygen exposure of methanogenic sludge. Water Sci Technol 48(6): 119–124

Fredrickson JK, Zachara JM, Kennedy DW, Dong H, Onstott TC, Hinman NW, Li SM (1998) Biogenic iron mineralization accompanying the dissimilatory reduction of hydrous ferric oxide by a groundwater bacterium. Geochim Cosmochim Ac 62:3239–3257

Fujii T, De Groot FMF, Sawatzky GA, Voogt FC, Hibma T, Okada K (1999) In situ XPS analysis of various iron oxide films grown by NO_2-assisted molecular-beam epitaxy. Phys Rev B 59(4):3195–3202

Gaspard S, Vazquez F, Holliger C (1998) Localization and solubilization of the Iron (III) reductase of *Geobacter sulfurreducens*. Appl Environ Microbiol 64:3188–3194

Ghanavati H, Nahvi I, Karimi K (2015) Organic fraction of municipal solid waste as suitable feedstock for the production of lipid by oleaginous yeast *Cryptococcus aerius*. Waste Manag https://doi.org/10.1016/j.wasman.2014.12.007

Garibay-Orijel C, Ríos-Leal E, García-Mena J, Poggi-Varaldo HM (2005) 2,4,6-Trichlorophenol and phenol removal in methanogenic and partially aerated methanogenic conditions in a fluidized bed bioreactor. J Chem Technol Biotechnol 80:1180–1187. https://doi.org/10.1002/jctb.1313

Ghimire A, Frunzo L, Pirozzi F, Trably E, Escudie R, Lens PNL, Esposito G (2015) A review on dark fermentative biohydrogen production from organic biomass: process parameters and use of by-products. Appl Energ 144:73–95

Graham HD (1992) Stabilization of the Prussian blue color in the determination of polyphenols. J Agric Food Chem 40:801–805

Guo H, Barnard AS (2013) Naturally occurring iron oxide nanoparticles: morphology, surface chemistry and environmental stability. J Mater Chem A 1:27–42

Habouzit F, Hamelin J, Santa-Catalina G, Steyer JP, Bernet N (2014) Biofilm development during the start-up period of anaerobic biofilm reactors: the biofilm Archaea community is highly dependent on the support material. Microb Biotechnol 7:257–264

Hennebel T, Verhagen P, Simoen H, De Gusseme B, Vlaeminck SE, Boon N, Verstraete W (2009) Remediation of trichloroethylene by bio-precipitated and encapsulated palladium nanoparticles in a fixed bed reactor. Chemosphere 76:1221–1225

Hernández-Correa E, Poggi-Varaldo HM, Ponce-Noyola MT, Solorza-Feria O, Romero-Cedillo L, Ríos-Leal E, Hernández-Flores G (2017) Powdered eggshell waste: adsorbent of inhibitors in hydrolysate of OFMSW. Segundo Congreso Internacional de Energía 2017. CDMX, México. 04-08 September 2017. Paper 119, pp. 1–6

Honary S, Barabadi H, Ebrahimi P, Naghibi F, Alizadeh A (2015) Development and optimization of biometal nanoparticles by using mathematical methodology: a microbial approach. J Nanopart Res 30:106–115. https://doi.org/10.4028/www.scientific.net/JNanoR.30.106

Hung CH, Lee KS, Cheng LH, Huang YH, Lin PJ, Chang JS (2007) Quantitative analysis of a high-rate hydrogen-producing microbial community in anaerobic agitated granular sludge bed bioreactors using glucose as substrate. Appl Microbiol Biotechnol 75:693–701

Jaafarzadeh N, Ghanbari F, Ahmadi M (2017) Catalytic degradation of 2, 4-dichlorophenoxyacetic acid (2,4-D) by nano-Fe2O3 activated peroxymonosulfate: influential factors and mechanism determination. Chemosphere 169:568–576

Jacob JJ, Suthindhiran K (2016) Magnetotactic bacteria and magnetosomes-scope and challenges. Mater Sci Eng C 68:919–928

Jiménez-Pérez JL, Sánchez-Ramírez JF, Cornejo-Monroy D, Gutierrez-Fuentes R, Rojas-Pescador JA, Cruz-Orea A, Algatti MA, Jacinto C (2012) Photothermal study of two different nanofluids containing SiO_2 and TiO_2 semiconductor nanoparticles. Int J Thermophys 33: 60–79

Judger BE, Ertan H, Bohl S, Lee M, Marquis CP, Manefield M (2016) Organohalide respiring bacteria and reductive dehalogenases: key tools in organohalide bioremediation. Front Microbiol 7. https://doi.org/10.3389/fmicb.2016.00249

Kaufmann F, Lovley DR (2001) Isolation and characterization of a soluble NADPH-dependent Fe(III) reductase from *Geobacter sulfurreducens*. J Bacteriol 183:4468–4476

Kastrinaki G, Lorentzou S, Karagiannakis G, Rattenbury M, Woodhead J, Konstandopoulos AG (2018) Parametric synthesis of iron-based nanoparticles via aerosol spray pyrolysis route. J Aerosol Sci 115: 96–107

Khin M, Nair AS, Babu VJ, Murugan R, Ramakrishna S (2012) A review on nanomaterials for environmental remediation. Energy Environ Sci 5:8075–8109

Kim YJ, Park CR (2002) Analysis of problematic complexing behavior of ferric chloride with N, N-Dimethylformamide using combined techniques of FT-IR, XPS and TGA/DTG. Inorg Chem 41(24): 6211–6216. https://doi.org/10.1021/ic011306p

Kim Y, Lee Y, Roh Y (2015) Microbial synthesis of iron sulfide (FeS) and iron carbonate ($FeCO_3$) nanoparticles. J Nanosci Nanotechnol 15: 5794–5797

Kim Y, Roh Y (2018) Effects of microbial growth conditions on synthesis of magnetite nanoparticles using indigenous Fe(III)-reducing bacteria. Minerals 8(5):212. https://doi.org/10.3390/min8050212

Kumar KS, Chen WS, Li L, Sung S (2006) Biohydrogen production in continuous-flow reactor using mixed microbial culture. Water Environ Res 78:110–117

Laurent S, Forge D, Port M, Roch A, Robic C, Vander Elst L, Muller RN (2008) Magnetic iron oxide nanoparticles: synthesis, stabilization, vectorization, physicochemical characterizations, and biological applications. Chem Rev 108:2064–2110

Leitao P, Aulenta F, Rosetti S, Nows HPA, Danko AS (2018) Impact of magnetite nanoparticles on the syntrophic dichlorination of 1,2-dichloroethane. Sci Total Environ 624:17–23

Lesiak B, Rangam N, Jiricek P, Gordeev I, Tóth J, Kövér L, Mohai M, Borowicz P (2019) Surface study of Fe3O4 nanoparticles functionalized with biocompatible adsorbed molecules. Front Chem 7:642

Li YS, Church JS, Woodhead AL (2012) Infrared and Raman spectroscopic studies on iron oxide magnetic nano-particles and their surface modifications. J Magn Magn Mater 324:1543–1550

Lim J, Yeap SP, Che HX, Low SC (2013) Characterization of magnetic nanoparticle by dynamic light scattering. Nanoscale Res Lett 8:381–395

Liu J, Römer I, Tang SVY, Valsami-Jones E, Palmer RE (2017) Crystallinity depends on choice of iron salt precursor in the continuous hydrothermal synthesis of Fe-Co oxide nanoparticles. RSC Adv 7(59):37436–37440

Lohner ST, Spormann AM (2017) Identification of a reductive tetrachloroethene dehalogenase in *Shewanella sediminis*. Philos T R Soc 368. https://doi.org/10.1098/rstb.2012.0326

Lovley DR, Giovannoni SJ, White DC, Champine JE, Phillips EJ, Gorby JA, Gorby YA, Goodwin S (1993) *Geobacter metallireducens* gen nov sp nov a microorganism capable of coupling the complete oxidation of organic compounds to the reduction of iron and other metals. Arch Microbiol 159:336–344

Ma J, Wang L, Wu Y, Dong X, Ma Q, Qiao C, Zhang Q, Zhang J (2014) Facile synthesis of Fe3O4 nanoparticles with a high specific surface area. Mater Trans 55:1900–1902

Machado S, Grosso JP, Nouws HPA, Albergaria JT, Delerue-Matos C (2014) Utilization of food industry wastes for the production of zero-valent iron nanoparticles. Sci Total Environ 496:233–240

Magnuson TS, Isoyama N, Hodges-Myerson AL, Davidson G, Maroney M, Geesey GG, Lovley DR (2001) Isolation, characterization and gene sequence analysis of a membrane-associated 89 kDa Fe (III) reducing cytochrome *c* from *Geobacter sulfurreducens*. Biochem J 359:147–152

Marzorati M, Ferra F, Van Raemdonck H, Borin S, Allifranchini E, Carpani G, Serbolisca L, Verstraete W, Boon N, Daffonchio D (2007) A novel reductive dehalogenase, identified in a contaminated groundwater enrichment culture and in *Desulfitobacterium dichloroeliminans* strain DCA1, is linked to dehalogenation of 1,2-Dichloroethane. Appl Environ Microbiol 73:2990–2999

Mayer-Blackwell K, Azizian MF, Green JK, Spormann AM, Semprin L (2017) Survival of vinyl chloride respiring *Dehalococcoides mccartyi* under long-term electron donor limitation. Environ Sci Technol 51:1635–1642

Miller GL (1959) Use of dinitrosalicylic acid reagent for determination of reducing sugar. Anal Chem 31:426–428

Montgomery DC (2017) Design and analysis of experiments, 9th edn. Wiley, New York 640 pp

Moreno-Medina CU, Poggi-Varaldo HM, Breton-Deval L, Rinderknecht-Seijas N (2017) Effect of sudden addition of PCE and bioreactor coupling to ZVI filters on performance of fluidized bed bioreactors operated in simultaneous electron acceptor modes. Environ Sci Pollut Res 24(33):25534–25549. https://doi.org/10.1007/s11356-016-7275-z

Moulder JF, Stickle WF, Sobol PE, Bomben KD (1992) Handbook of X-ray photoelectron spectroscopy. Minnesota USA 254:81–82

Muñoz-Páez KM, Ruiz-Ordaz N, García-Mena J, Ponce-Noyola MT, Ramos-Valdivia AC, Robles-González IV, Villa-Tanaca L, Barrera-Cortés J, Rinderknecht-Seijas N, Poggi-Varaldo HM (2013) Comparison of biohydrogen production in fluidized bed bioreactors at room temperature and 35 °C. Int J Hydrogen Energ 38:12570–12579

Noguchi Y, Fujiwara T, Yoshimatsu K, Fukumori Y (1999) Iron reductase for magnetite synthesis in the magnetotactic bacterium *Magnetospirillum magnetotacticum*. J Bacteriol 181:2142–2147

Oza M, Joshi MJ (2017) Hydrothermal synthesis of siderite nanoparticles and characterizations. Functional Oxides and Nanomaterials AIP Conf. Proc. 1837, 040037-1-0400; https://doi.org/10.1063/1.4982121

Pérez-González M, Tomás SA, Santoyo-Salazar J, Gallardo-Hernández MM, Téllez-Cruz MM, Solorza-Feria O (2018) Sol-gel synthesis of Ag-loaded TiO_2-ZnO thin films with enhanced photocatalytic activity. J Alloys Compd 779:908–917

Piccinno F, Hischier R, Seeger S, Som C (2018) Predicting the environmental impact of a future nanocellulose production at industrial scale: application of the life cycle assessment scale-up framework. J Clean Prod 174:283–295

Poggi-Varaldo HM, Oleszkiewicz JA (1992) Anaerobic co-composting of municipal solid waste and waste sludge at high total solids levels. Environ Technol 13(5):409–421

Poggi-Varaldo HM, Munoz-Paez KM, Escamilla-Alvarado C, Robledo-Narváez PN, Ponce-Noyola MT, Calva-Calva G (2014) Biohydrogen, biomethane and bioelectricity as crucial components of biorefinery of organic wastes: a review. Waste Manag Res 32:353–365

Poggi-Varaldo HM, Bárcenas-Torres JD, Moreno-Medina CU, García-Mena J, Garibay-Orijel C, Ríos-Leal E, Rindercknecht-Seijas N (2012) Influence of discontinuing feeding degradable co-substrate on the performance of a fluidized bed bioreactor treating a mixture of trichlorophenol and phenol. J Environ Manag 113:527–537

Poulin S, Franca R, Moreau-Bélanger L, Sacher E (2010) Confirmation of X-ray photoelectron spectroscopy peak attributions of nanoparticulate iron oxides, using symmetric peak component line shapes. J Phys Chem C 114:10711–10718

Radu T, Iacovita C, Benea D, Turcu R (2017) X-ray photoelectron spectroscopic characterization of iron oxide nanoparticles. Appl Surf Sci 405:337–343

Ramírez-Nuñez AL, Jiménez-García LF, Goya GF, Sanz B, Santoyo-Salazar J (2018) In vitro magnetic hyperthermia using polyphenol-coated Fe_3O_4 and Fe_2O_3 nanoparticles from Cinnamomum verum and Vanilla planifolia: the concert of green synthesis and therapeutic possibilities. Nanotechnology 29:18–37

Ripley LE, Boyle WC, Converse JC (1986) Improved alkalimetric monitoring for anaerobic digestion of high-strength waste. J Water Pollut Control Fed 58(5):406–411

Ristic M, Krehula S, Reissner M, Music S (2017) ^{57}Fe Mossbaüer, XRD, FT-IR, FE SEM analyses of natural goethite, hematite and siderite. Croat Chem Acta 90(3):499–507

Robledo-Narváez PN, Muñoz-Páez KM, Poggi-Varaldo HM, Ríos-Leal E, Calva-Calva G, Ortega-Clemente LA, Rinderknecht-Seijas N, Estrada-Vázquez C, Ponce-Noyola MT, Salazar-Montoya JA (2013) The influence of total solids content and initial pH on batch biohydrogen production by solid substrate fermentation of agroindustrial wastes. J Environ Manag 128:126–137

Roh Y, Liu SV, Li G, Huang H, Phelps TJ, Zhou J (2002) Isolation and characterization of metal-reducing *Thermoanaerobacter* strains from deep subsurface environments of the Piceance Basin, Colorado. Appl Environ Microbiol 68:6013–6020

Ross DE, Ruebush SS, Brantley SL, Hartshorne RS, Clarke TA, Richardson DJ, Tien M (2007) Characterization of protein-protein interactions involved in iron reduction by *Shewanella oneidensis* MR-1. Appl Environ Microbiol 73:5797–5808

Safarik I, Pospiskova K, Baldikova E, Safarikova M (2016) Development of advanced biorefinery concepts using magnetically responsive materials. Biochem Eng J 116:17–26

Samaddar P, Ok YS, Kim KH, Kwon EE, Tsang DCW (2018) Synthesis of nanomaterials from various wastes and their new age applications. J CleanProd 197:1190–1209

Santillán J, Williams Q (2004) A high-pressure infrared and X-ray study of $FeCO_3$ and $MnCO_3$ comparison with CaMg $(CO_3)_2$-dolomite. Phys Earth Planet Inter 143:291–304

Saranya T, Parasuraman K, Anbarasu M, Balamurugan K (2015) XRD, FT-IR and SEM study of magnetite (Fe_3O_4) nanoparticles prepared by hydrothermal method. Nano Vision 5:149–154

Sardjono RE, Khoerunnisa F, Musthopa I, Qowiyah A, Khairunisa D, Erfianty DD, Rachmawati R (2018) Biosynthesis, characterization and anti-Parkinson activity of magnetite-Indonesian velvet beans (*Mucuna pruriens L.*) nanoparticles. J Eng Sci Technol 13(12): 4258–4270

Satari B, Karimi K (2018) Citrus processing wastes: environmental impacts, recent advances, and future perspectives in total valorization. Resour Conserv Recycl 129:153–167

Seabra AB, Haddad P, Duran N (2013) Biogenic synthesis of nanostructured iron compounds: applications and perspectives. IET Nanobiotechnol 7:90–99

Sikora A, Blaszczyk M, Jurkowski M, Zielenkiewicz U (2013) Lactic acid bacteria in hydrogen-producing consortia: on purpose or by coincidence? Chapter 21. Lactic acid bacteria-R&D for food, health and livestock purposes. Intech Open. https://doi.org/10.5772/50364

Sotelo-Navarro PX, Poggi-Varaldo HM, Turpin-Marion SJ, Vázquez-Morillas A, Beltrán-Villavicencio M, Espinosa-Valdemar RM (2017) Biohydrogen production from used diapers: evaluation of effect of temperature and substrate conditioning. Waste Manag Res 35(3):267–275

Staniland SS, Ward B, Harrison A (2009) Biosynthesis of magnetite by microbes. Chapter 21 in *Neutron* applications in earth energy and environmental sciences, neutron scattering applications techniques. https://doi.org/10.1007/978-0-387-09416-8 21, pp. 595-618

Sundaram PA, Augustine R, Kannan M (2012) Extracellular biosynthesis of iron oxide nanoparticles by *Bacillus subtilis* strains isolated from rhizosphere soil. Biotechnol Bioproc Eng 17:835–840

Thunugunta T, Reddy AC, Reddy DCL (2015) Green synthesis of nanoparticles: current prospectus. Nanotechnol Rev 4:303–323

US Environmental Protection Agency (2006) National perchloroethylene air emission standards for dry cleaning facilities – part II: final rule. Washington D.C, USEPA, Federal Register, 40 CFR Part 63

US Environmental Protection Agency (2017) Scope of the risk evaluation for perchloroethylene. CASRN:127-18-4. EPA Document #EPA-740-R1-7007

Vilaplana F, Strömberg E, Karlsson S (2010) Environmental and resource aspects of sustainable biocomposites. Polym Degrad Stab 95:2147–2161

World Health Organization (2000) Air quality guidelines. In: Chapter 5.13: tetrachloroethylene, 2nd edn. Regional Office for Europe, Copenhagen

Wu X, Lu S, Qiu Z, Sui Q, Lin K, Du X, Luo Q (2014) The reductive degradation of 1,1,1-trichloroethane by Fe (0) in a soil slurry system. Environ Sci Pollut Res 21:1401–1410

Xin J, Tang F, Yan J, La C, Zheng X, Liu W (2018) Investigating the efficiency of microscale zero valent iron-based in situ reactive zone (mZVI-IRZ) for TCE removal in fresh and saline groundwater. Sci Total Environ 626:638–649

Yadav M (2018) Study on thermal and mechanical properties of cellulose/iron oxide bionanocomposites film. Composite Commun 10:1–5

Yan L, Da H, Zhang S, Morillo-López V, Wang W (2017) Bacterial magnetosome and its potential application. Microbiol Res 203:19–28

Yang P, Zhang R, McGarvey JA, Benemann JR (2007) Biohydrogen production from cheese processing wastewater by anaerobic fermentation using mixed microbial communities. Int J Hydrogen Prod 32:4761–4771

Yeary LW, Moon JW, Love LJ, Thompson JR, Rawn CJ, Phelps TJ (2005) Magnetic properties of biosynthesized magnetite nanoparticles. IEEE Trans Magn 41:4384–4389

Zhong YH, Yu L, Chen ZF, He H, Ye F, Cheng G, Zhang Q (2017) Microwave-assisted synthesis of Fe3O4 nanocrystals with predominantly exposed facets and their heterogeneous UVA/Fenton catalytic activity. ACS Appl Mater Interfaces 9:29203–29212. https://doi.org/10.1021/acsami.7b0692Zhong